INTERFEROMETRIC STUDIES OF LAMINAR AND TRANSITIONAL FREE CONVECTION HEAT TRANSFER IN WATER

A THESIS

Presented to

The Faculty of the Division of Graduate

Studies and Research

By

Jayesh Mehta

In Partial Fulfillment

of the Requirements for the Degree

Master of Science in Mechanical Engineering

Georgia Institute of Technology

August, 1975

INTERFEROMETRIC STUDIES OF LAMINAR AND TRANSITIONAL FREE CONVECTION HEAT TRANSFER IN WATER

Approved:

W. Z. Black, Chairman

D. C. Oshea

Thomas W. Jackson

Date approved by Chairman: 8/8/75

ACKNOWLEDGMENTS

I would like to express my deepest gratitude to all those who have assisted in the completion of this thesis. I take this opportunity to convey my special thanks to Dr. William Z. Black, who generously gave his advice and time. My thanks go to several technicians, especially to Mr. George Halstead and to Mr. G. E. Clompton, for constructing the test apparatus.

Finally, I express my thanks to the School of Mechanical Engineering for funding the test equipment and awarding me the financial support during the period of my studies at Georgia Tech.

TABLE OF CONTENTS

TABLE OF CONTENTS (Concluded)

LIST OF TABLES

LIST OF TABLES (Concluded)

LIST OF ILLUSTRATIONS

LIST OF ILLUSTRATIONS (Concluded)

NOMENCLATURE

Symbol	Definition	Units
a_k	knife edge parameter	ft
C	proportionality constant	dimensionless
$dn/dT, (dn/dT)_w$	refractive index gradient with temperature, gradient at the wall	1/°C
e_{end}	percent end effect error	dimensionless
e_{ref}	percent refraction error	dimensionless
g	distance between WP1 and the spherical mirror	ft
Gr_x	local Grashof number	dimensionless
h_x	local heat transfer coefficient	Btu/hr-ft^2-°F
$\Delta I/I_0$	relative contrast for Schlieren and shadowgraph systems	dimensionless
k	modified Gladstone-Dale constant	°R
k_f	thermal conductivity of fluid	Btu/hr-ft-°F
L	width of the test plate	ft
ΔL_{ref}	error in optical path length due to refraction	ft
Δl_{ref}	error in optical path length for differential interferometer	ft
m	fringe deflection at the surface	dimensionless
Nu_x	local Nusselt number	dimensionless
n	refractive index	dimensionless
n_a	refractive index at the ambient temperature	dimensionless
(n_e-n_0), Δn	difference between the extraordinary and ordinary index of refrac-	dimensionless

NOMENCLATURE (Continued)

Symbol	Definition	Units
	tion of bifringent material	
Pr	Prandtl number of the fluid	dimensionless
q/A	heat input to the plate	Btu/hr-ft^2
Ra_x	local Rayleigh number	dimensionless
T	local temperature inside the boundary layer	°C, °F
T_a	ambient temperature condition	°C, °F
T_w	surface wall temperature	°C, °F
(T_w-T_a), ΔT	difference between the wall and ambient temperature	°C, °F
$T_{\Delta X_s}$	temperature at a distance ΔX_s away from the plate	°C, °F
x	distance to the plate from leading edge	ft
y	perpendicular distance from the plate to the boundary layer	ft
z	distance along the path of the ray	ft
α	total angle of deflection of ray x and ray y defined by equation 2	radians
α_w	ratio of the distance of the focal plane from camera to the width of the test section	dimensionless
δ	boundary layer thickness	ft
ΔX_s	separation distance between ray x and ray y in the test section	ft
θ	nondimensional temperature $(T-T_w)/(T_w-T_a)$	dimensionless
θ_i	wedge angle of the Wollaston prism	radians

NOMENCLATURE (Concluded)

Symbol	Definition	Units
λ	wavelength of light	Angstrom (Å)
ϕ	nondimensional temperature $(T-T_w)/T_w$	dimensionless

SUMMARY

An optical device called the differential interferometer was applied to free convection heat transfer in laminar, transitional, and turbulent regimes. Heat transfer coefficients were measured over a two foot long, vertical, isothermal aluminum plate. Water was used as a transport medium for all the experimental runs. Error analysis was performed for the differential as well as the Mach-Zehnder interferometer.

The results for low Grashof numbers are presented in graphical form. A good agreement was found with available theoretical results. The maximum Rayleigh number achieved for steady state results was 8.79×10^8.

The results for higher Grashof numbers were found to deviate considerably from theoretical data due to refraction.

Infinite fringe patterns were used to study the transition of the flow from laminar to turbulent. The boundary layer was found to have a double structure where, at highest Grashof numbers, the vortices in the outer layer controlled the flow completely. The inner layer was affected by a large amplification of the disturbance in the outer layer, which overtakes the flow completely and results in the breakdown of the free convection layer from laminar to turbulent.

An analytical investigation was initiated to study various errors involved in the interferometric measurements. End effect errors, as well as refraction errors, were evaluated as a function of various parameters for Mach-Zehnder and differential interferometers applied to air and water.

End effect errors were found to be less for the differential interferometer than for the Mach-Zehnder interferometer. For air studies the refraction error was considerably less for the differential interferometer than for the Mach-Zehnder interferometer. However, for water studies, the difference in the refraction error for these two interferometers was small.

CHAPTER I

INTRODUCTION

Free convection has been the subject of many theoretical and experimental investigations for many years. This study reports on a basic study of free convection in liquids from vertical surfaces. The measurement technique utilizes an optical device known as a differential interferometer. The primary objective of this investigation was to apply an optical technique to a heat transfer problem involving liquids, since very few studies have successfully achieved accurate, clear interference patterns when liquid is used as a transport medium. The secondary objective of this investigation was to study the detailed structure of the fluid motion in the layer of a heated fluid, adjacent to the surface.

Basically, free convection is a transport mechanism in which the fluid motion is generated by the interaction of two effects: buoyancy and gravitational. Normally the buoyancy effect is generated by a change in the temperature field. Such temperature induced density gradients are observed in atmospheric circulations, oceanic undercurrents, and in the familiar room heating systems. Free convection may further be classified as laminar, transitional, and turbulent.

The fundamental difference between free and forced convection flows involves the manner in which the flow is generated. The forced convection flows are induced because of an external driving force. Free convection flows are induced due to a driving force caused by fluid temperature

differences. In general, solutions for free convection heat transfer problems are more difficult than for purely forced convection flows. The difficulties involved in free convection can be ascribed to small velocities encountered which result in the same order of magnitude of the momentum and the viscous effects. Furthermore, the velocity and the temperature fields are coupled and dependent upon each other, making the solution to the governing differential equations quite involved.

Interferometers have been used often to measure the temperature distribution in the fluid adjacent to a heated surface. The most frequently used device is the Mach-Zehnder interferometer. Most of these studies have involved measurements in a gas, usually air. The application of interferometers to the measurement of temperature distribution in liquids is a great deal more involved because of the scattering of light in the liquid, because of larger index of refraction changes resulting from relatively small temperature differences, and difficulties in containing the liquid in optically flat surfaces which do not introduce any interference patterns of their own.

The differential interferometer is an instrument which has become available recently even though the principle of its operation has been known for several decades. Its application to the heat transfer research has been limited because of the acceptability and success of the Mach-Zehnder interferometer. However, the differential interferometer possesses several advantages that make its application to heat transfer measurements more desirable than the Mach-Zehnder interferometer.

One of the advantages of the differential interferometer is that it

allows the study of the heat transfer mechanism quantitatively as well as qualitatively with only one setting. Depending upon the insertion of the third Wollaston prism, the interferograms produce either parallel or infinite fringe patterns. Furthermore, the differential interferograms can be directly related to the temperature gradient at the heated surface. Therefore, there is no need to locate the isotherms and approximate the temperature gradients in order to determine the heat transfer coefficients. The only measurement necessary is the relative displacement of an individual fringe line at the surface. Therefore, the differential interferometer provides a simpler means of measuring heat transfer than does the Mach-Zehnder interferometer.

Statement of Problem

The purpose of this research is to study the application of the differential interferometer to an experimental study of the free convection flow over a vertical isothermal flat plate submerged in a liquid. Water was selected as a transport medium, since its optical and thermal properties are well documented in the literature. A simple geometry of a vertical flat plate was selected because the availability of other experimental results in the literatuve made the job of determining the accuracy of this technique much easier.

The present investigation was carried out with the objectives of:

1. Demonstrating the potential of the differential interferometer to the measurement of the free convection heat transfer in a medium other than air. This objective was achieved by determining the heat transfer coefficient for the proposed geometry as a function of height as well as

the temperature difference between the ambient fluid and wall.

2. Studying the structure of the boundary layer qualitatively and determining the frequency of occurrence of the thermal waves in transitional and turbulent regimes.

3. Studying the optical errors in the interferometric measurements and comparing the end effect and refraction errors for the differential interferometer with the Mach-Zehnder interferometer.

4. Determining the critical Rayleigh numbers which mark the onset of the transition regime.

Review of Literature

Over the past several decades, heat transfer over a flat plate, vertical, and inclined positions and with isothermal and uniform heat fluxes has been a subject of many investigations. Most of this work is on the determination of either the average heat transfer coefficient, the velocity profile, or the temperature distribution in the thermal boundary layer. The following section summarizes the major papers on this subject.

Steady State--Theoretical

Even though a large amount of experimental and empirical knowledge had been acquired during the 19th century, it was only during the last quarter of the 19th century that an organized attempt was made to obtain a solution to the problem of free convection. In 1881, Lorenz (1) published a solution to free convection flow over a vertical flat plate surrounded by air.

Subsequent efforts to improve the analytical results of Lorenz led Schmidt and Beckman (2) to propose the equation for heat transfer coeffi-

cient in terms of a power law, such as, $Nu_x = C(Gr_x Pr)^n$. The system of equations was numerically integrated for air by E. Polhausen (3) using the experimental data. The resulting constants were 0.497 and 0.25 for C and n, respectively. The power law was valid only in the laminar range and could not be used for any transport medium other than air.

In 1936, Saunders (4) performed an analysis which gave the analytical solutions that were not dependent upon any experimental values. Saunders also compared the theoretical values with the experimental data for an isothermal vertical plate submerged in water. For turbulent flow, the results were compiled in the form of a power law, $(Nu_x) = C(Gr_x Pr)^n$. The numerical values of $C = 0.17$ and $n = 0.333$ matched very well with the experimental results for $Pr = 7.0$.

In 1951, Eckert and Jackson (5) reported a theoretical analysis of the turbulent free convection boundary layer. The method used Von Karman's integral momentum and energy boundary layer equations, data on the forced convection wall shearing stress, and heat transfer from forced convection flow. Furthermore, it was assumed that the turbulent flow initiated from the leading edge of the plate, thus covering only the developed, fully turbulent boundary layer.

Apparently, Ostrach (6) was the first investigator to report an extensive set of values for an isothermal plate over a wide range of Prandtl numbers. Numerical solutions were obtained to the governing differential equations for the Prandtl numbers ranging from 0.01 to 1000.

Steady State--Experimental

An experimental investigation of the free convection problem was made by Griffiths and Davis (7) in 1922. The experimental apparatus

consisted of a uniformly heated plate, 50 inches square, hung vertically in air. The results substantiated the Lorenz results that the film coefficient of the heat transfer was proportional to the fourth root of the temperature difference between the plate and the ambient air. In the course of the experiment the temperature and velocity fields were determined with the help of a combination hot wire anemometer and a resistance thermometer.

It was Saunders (4) who first reported an experimental value for a fluid other than air. Prior to Saunders, the only experiments on natural convection in liquids were those of Lorenz, who measured mean heat loss from a plate submerged in oil. Saunders measured the heat loss from a heated vertical plate in water, for laminar and turbulent flow conditions. The experimental results agreed very well with the theoretical predictions.

Dotson (8) presented a complete set of experimental values of local heat transfer coefficients for a uniformly heated plate submerged in water. The effect of the starting length on heated surfaces was also investigated. Dotson concluded that if a horizontal surface is placed eight inches or more below the lower edge of the plate, then it should not have any effect on the temperature distribution of the plate.

Tetsu Fujii (9) investigated free convection heat transfer from a vertical cylinder of 360 mm in height and 76 mm in diameter to ethylene glycol and water. The experimental results were correlated by a power law such as, $Nu = 0.65\ (Gr\ Pr)^{n}$, where $n = 0.25$ for laminar range and $Nu = 1.16\ (Gr\ Pr)^{0.2}$ - 155 for the turbulent range. The development of the boundary layer from laminar to turbulent through transition was also studied. Fujii concluded that the boundary layer develops through a

laminar, vortex street, transition-turbulent, and turbulent flow pattern with each flow pattern having respective characteristics of heat transfer. With respect to water, however, no distinction was found between transition-turbulent and turbulent flow.

Recently, Goldstein (10) used the Mach-Zehnder interferometer to study the steady state and transient free convection boundary layer along a uniformly heated vertical plate. Air as well as water was used as a transport medium. The experiments were performed when the plate was immersed in water. The steady state boundary layer as well as its transient development from an initial uniform temperature state to steady state condition was investigated when a step function power input was applied to the plate. Results for the steady state runs agreed very well with the results of an analysis by Sparrow (25). Using the experimental values at a distance x for which the heat flow is locally constant, an average value of 0.513 was obtained for the parameter $Nu/(Gr\ Pr)^{0.25}$. This compares with the value 0.5146 resulting from theoretical analysis.

Transient Studies

The stability of a fluid adjacent to a heated surface has been the subject of many recent studies. However, one of the earliest investigations on the transition from laminar to turbulent flow came from Saunders (4), who used a simple optical technique to determine the critical Rayleigh number which marks the onset of turbulence.

Interferometric studies of the same configuration made by Eckert (11) revealed for the first time that the turbulence was caused by the amplification of initially small disturbances. Recently, Szewczyk (12) confirmed and extended the work of Eckert, suggesting that the phenomenon

was not only two dimensional, but that spanwise effects were also important. These effects in turn were found to cause a sublayer, under which concentrated turbulent bursts are produced. These bursts increase with Grashoff number until completely turbulent flow results.

In 1968, Lock and Trotter (13) studied the structure of a turbulent free convection boundary layer in water. The study consisted of the local and overall structure of the mean boundary layer in terms of the fluctuations and frequency distributions and their relationships to mean profiles. The development of the thermal boundary layer, from laminar to turbulent through transition, was represented in terms of the temperature profiles which show a steepening as the flow becomes progressively turbulent. The observations led Lock and Trotter to conclude that the structure of a turbulent free convection boundary layer is quite different in terms of scale and intensity from the corresponding forced layer.

Recently, C. P. Black (14) investigated the thermal structure of a free convection boundary layer from an inclined isothermal plate in air. The experiments were conducted at 0, 10, 20, 35, and 40 degrees from vertical. It was observed that the frequencies of wave occurrences in the transitional regime are unstable; whereas the frequencies in the turbulent regime are quite stable. Furthermore, the passage of a thermal wave was found to cause a substantial decrease in the local heat transfer coefficient compared to the immediate downstream coefficient. In the transitional as well as the turbulent flow regimes, the thermal boundary layer was found to have a double structure. A thin thermal sublayer of almost a constant thickness was observed close to the plate. In the outer layer or the core region of varying thickness, the temperature profile was

found to vary rapidly. For the vertical plate, a vortex motion near the interface between the inner and outer layers was also observed.

Optical Techniques

The applications of the optical devices, especially using the shadowgraph, Schlieren, and interferometric techniques applied to study heat transfer in gases are quite well known. Consequently, this extensive literature will not be reviewed here. However, applications of optical devices to liquid heat transfer measurements have been rather few and these papers will be discussed briefly.

Saunders (4) used a simple optical technique to determine the critical Rayleigh number which marks the onset of turbulence. The technique consisted of observing the angular deflection of a beam of light very near to the plate. For steady streamline motion the deflection shown on the screen for any point on the plate was constant, but for unsteady flow it varied with time.

Apparently, B. Azami (15) was the first to use a Mach-Zehnder interferometer to study heat transfer in liquids. One of the water tanks had a small vertical aluminum strip which was heated, while the other tank was to act as a compensating tank. The experimental data on the temperature distribution in the boundary layer were checked using thermocouples. Agreement was found within 10 to 35 percent. However, no attempt was made to evaluate the heat transfer coefficients. The investigation failed to take into account the errors due to refraction and the errors due to end effect were incorrectly assumed to be negligible.

R. J. Goldstein (10) studied a free convection boundary layer using the Mach-Zehnder interferometer. End effect error and refraction

error were evaluated for the experimental system. They were found to be 0.5 percent and 1.6 percent, respectively. However, no attempt was made to study the transition from laminar to turbulent flow.

While the Mach-Zehnder interferometer has been used quite extensively in heat transfer research, the differential interferometer has been used sparsely in heat and mass transfer research. Bryngdhal (16) used the differential interferometer in the measurement of thermal conductivity of liquids. Black and Carr (17) applied the differential interferometer to the measurement of heat transfer coefficients from a vertical heated plate suspended in air. The sensitivity, accuracy, and validity of the technique were established comparing the results with the previous observations. A detailed description of this instrument and its various applications to heat and mass transfer research can be found in references 14, 16 and 19.

Application of the differential interferometer to heat transfer measurements has been limited, and the full potential of this instrument in the area of heat transfer has not been determined yet. One of the objectives of the present investigation was to determine the potential of the differential interferometer when applied to heat transfer measurements in liquids.

CHAPTER II

TEST APPARATUS

The test apparatus consists of four basic elements: water tank, flat plate, temperature measurement and power supply systems, and the camera and interferometer. Each element of the apparatus is discussed in detail in the sections which follow.

Water Tank

The tank was built from one half inch thick plexiglass. Two lateral walls of the tank were made of three pieces of one fourth inch optically flat glass while one of the side walls supported the heated plate which was a 24 by 6 inch aluminum plate with a thickness of one fourth inch. An 18" x 6.75" x 0.5" base plate supported the walls. As shown in Figure 1, a 1/4" by 1/4" groove was milled in the base plate which received the 1/4" by 1/4" tongue surfaces milled on the vertical walls. The heated aluminum plate was attached between the two vertical surfaces by 16 screws on each side and sealed with a rubber sealant.

The side walls of the tank were built with six 7.75" x 6" x 0.25" optically flat glass panels and eight supporting pieces. Grooves were milled on the supporting pieces so that the one fourth inch thick glass panels were supported on all four sides. The 1/4" by 1/4" extended surfaces on the supporting pieces allowed each piece to slide between the opposing faces of the vertical walls.

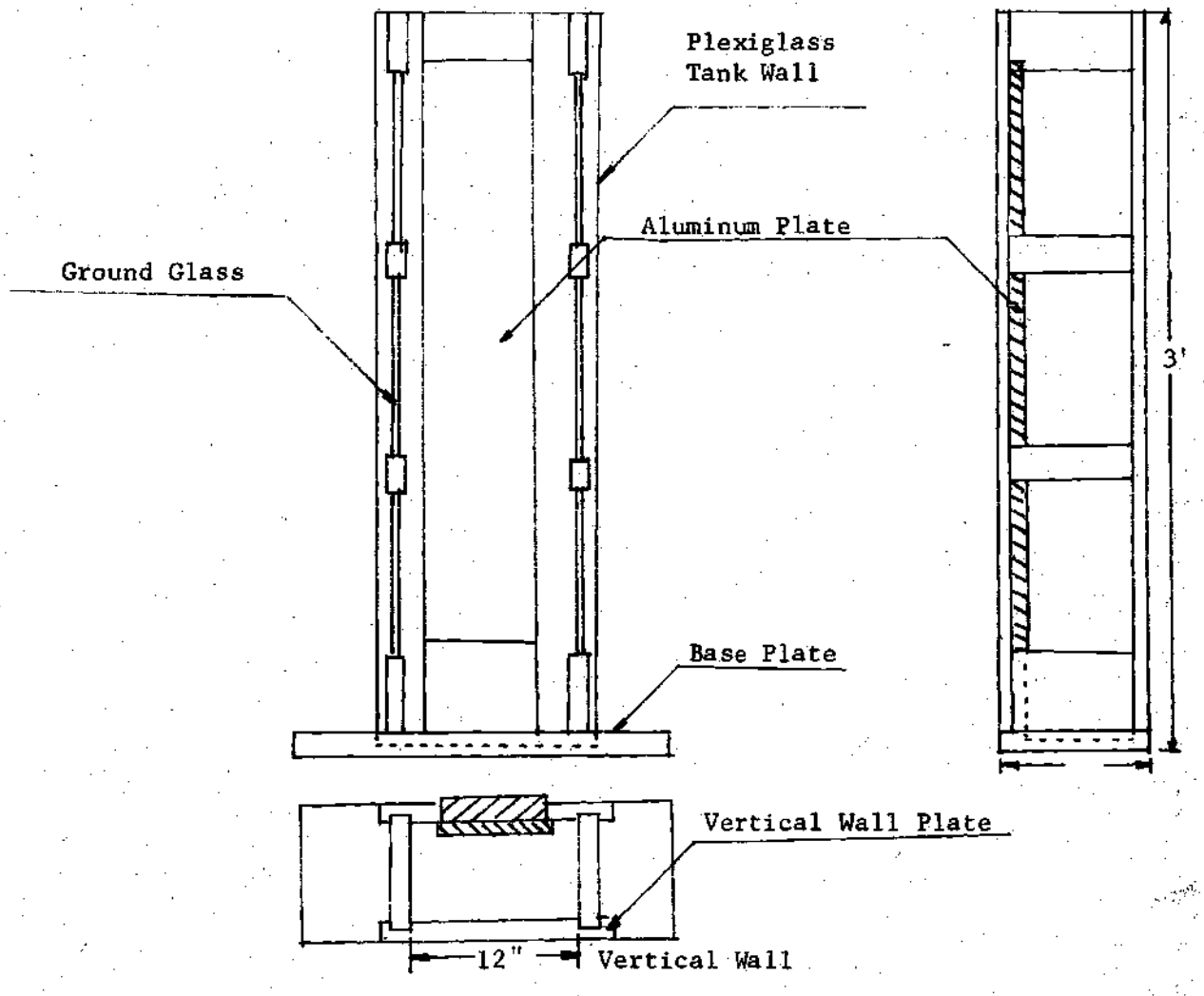

Figure 1. Schematic Diagram of the Test Tank

The internal dimensions of the tank were 36" x 12" x 6". The size of the tank was selected for several reasons. The capacity of the tank was 11.22 gallons and it contained 93.45 pounds of water. It was found that assuming the complete dissipation of a typical power input of 0.3 kw into the water did not raise the water temperature appreciably to affect the assumption of steady state operation. Furthermore, the width of the tank was selected such that it was much larger than the anticipated maximum boundary layer thickness. The theoretical value of the boundary layer thickness was calculated using the relationship:

$$\frac{\delta}{X} = 3.93\ (Pr)^{-0.5}\ (0.952+Pr)^{0.25}\ (Gr_x)^{-0.25}. \qquad (1)$$

Assuming the anticipated local Grashof number to be 10^6 and the Prandtl number to be 5.7, the maximum boundary layer thickness was anticipated to be 0.83 inch.

The test tank was constructed of 22 pieces including six glass panels. Therefore, there were numerous joints that had to be made waterproof. Three different kinds of cement were used for different mating surfaces. All plexiglass surfaces were joined with "Daybound thickened cement." General Electric "Kwik-Seal" cement was used for all aluminum to plexiglass surfaces. The Dow-Corning 781 building cement was used to seal the plexiglass to glass surfaces.

Flat Plate

The test surface was a 24" x 5" x 1/4" flat aluminum plate. It was held between two plexiglass walls by means of 16 screws on each side,

and supported by a plexiglass piece at the bottom. The mating edge of the plexiglass piece was beveled toward the back side of the plate. The gap between the aluminum plate and the mating plexiglass edge was filled with "Kwik-Seal" sealant, thus giving a waterproof joint. Since the leading edge of the heated plate was mounted flush with the plastic wall, the influence of the leading edge was minimized (20). The surface of the plate was polished to a smooth finish and care was taken to remove all protrusions and burrs from the surface of the plate.

Figure 3 shows the schematic diagram of the heater arrangement placed on the back of the plate. As shown in the diagram the plate was heated by means of "Watlow electric" silicone rubber heaters, attached to the rear surface of the aluminum plate. Since the heat transfer coefficient for an isothermal plate decreases with the distance from the leading edge, it was necessary to supply reduced power to the heaters mounted further from the leading edge. This was achieved by connecting each heater independently with its own variac, so that each heater could be controlled separately. The rear surfaces of the heaters were covered with one half inch fiberglass insulation in order to minimize the heat loss from the back surface of the plate.

Figure 1 depicts the schematic presentation of the test tank with the actual dimensions. Figure 2 is a photograph showing the test tank when positioned in the test region of the interferometer.

Temperature Measurements and the Power Supply

The main components of the temperature sensing system were copper-constantan thermocouples, a 24 channel Honeywell strip recorder, and a

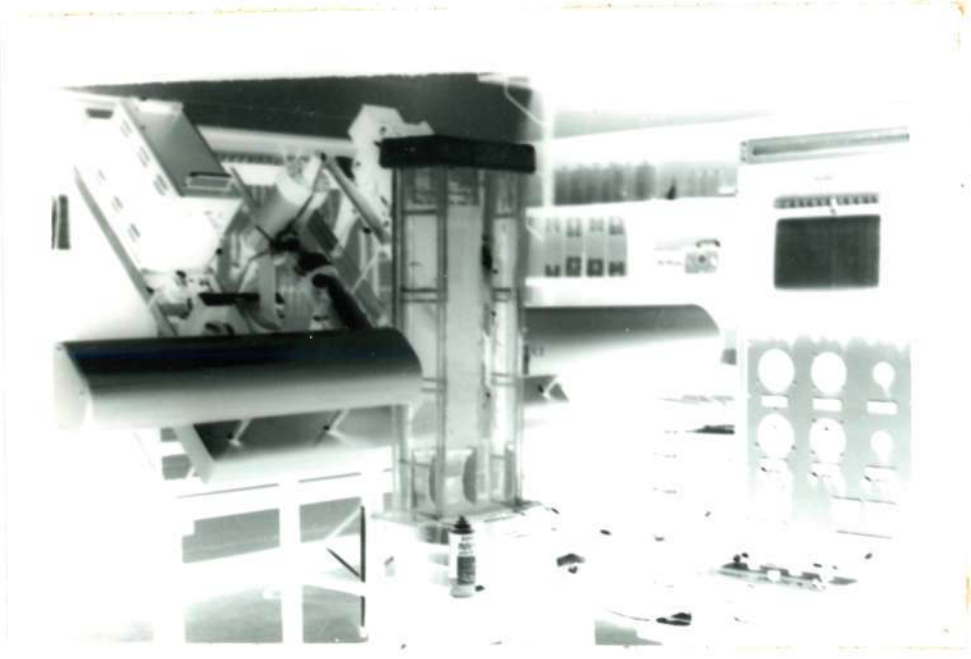

Figure 2a. Test Tank with the Heaters and the Temperature Measuring Device

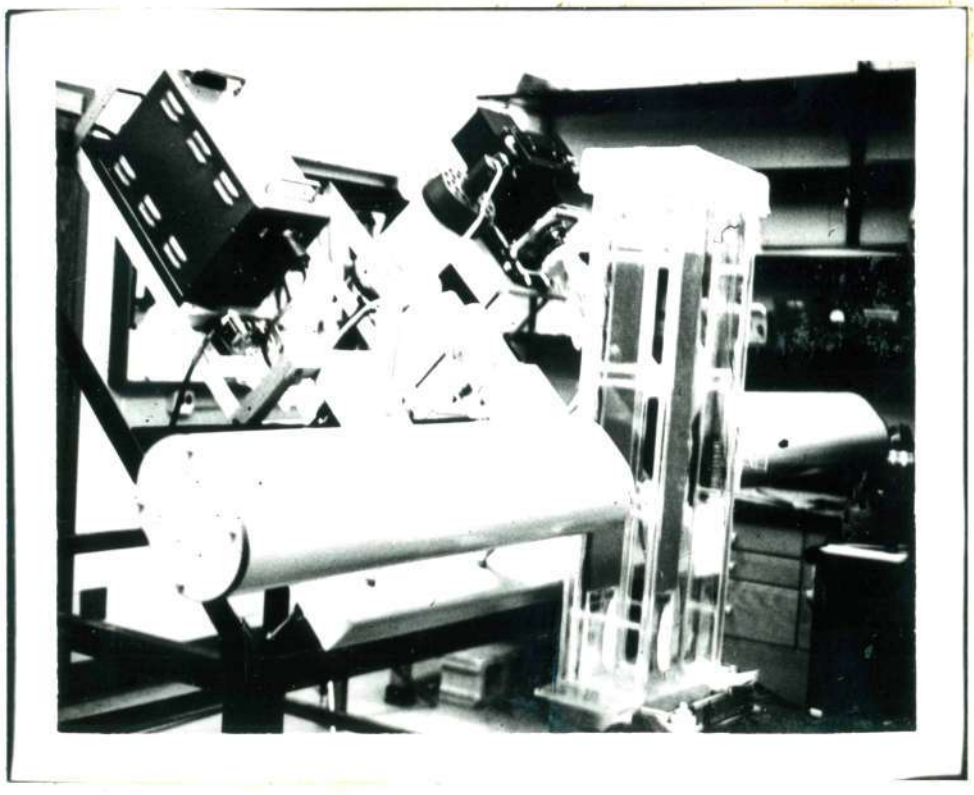

Figure 2b. Test Tank with a Bolex, 16 mm Movie Camera

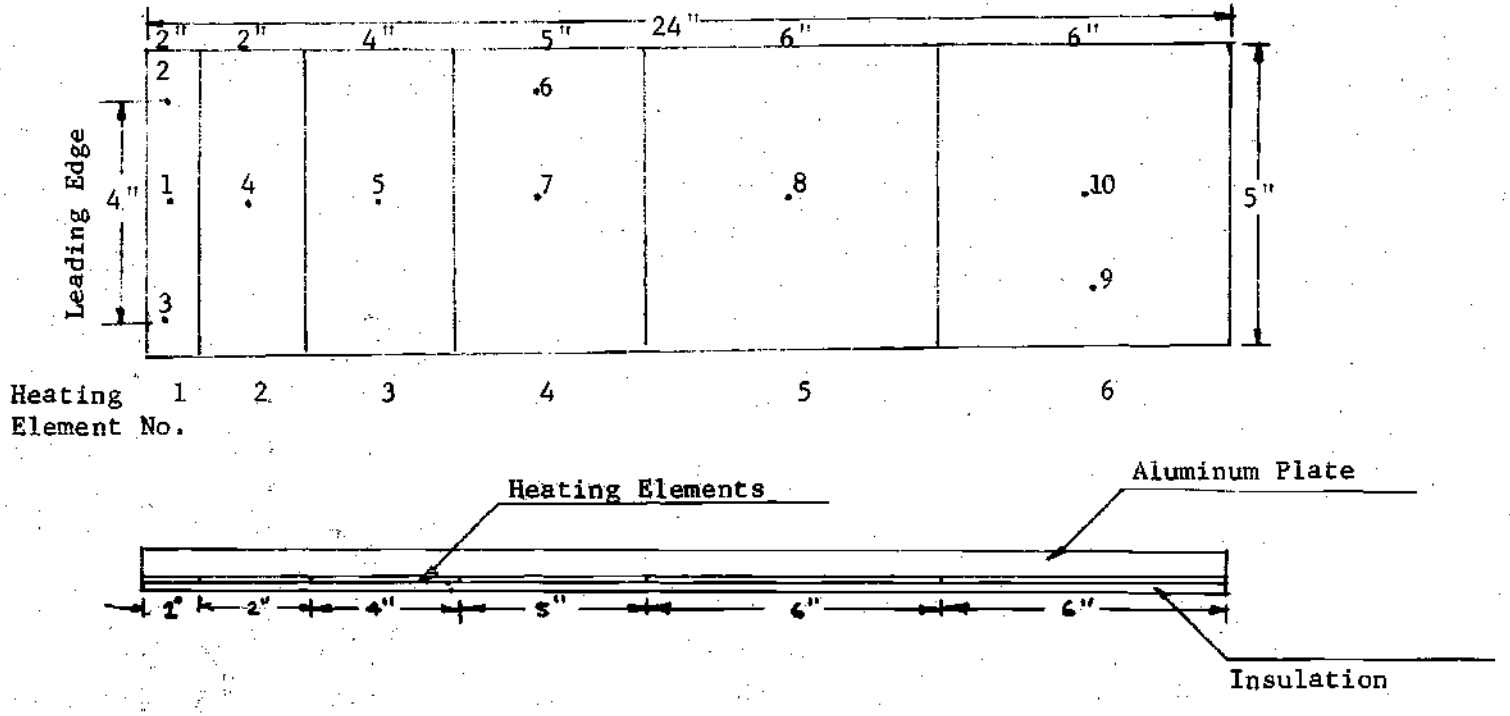

Figure 3. Aluminum Plate and Heating Elements

Leeds and Northrup millivolt potentiometer. As depicted in Figure 3, a total of ten thermocouples was mounted at the back of the plate. Six were attached such that each thermocouple was under the center of each heater. Two thermocouples at one half inch from the leading edge were located two inches off the central axis of the plate. One of the remaining two thermocouples was located at nine and one half inches from the leading edge and two inches off the central axis, and the other was mounted at 21 inches from the leading edge and two inches off the central axis. The off center thermocouples were used to determine the temperature variation across the width of the plate.

All thermocouples were positioned into the 0.035" x 0.053" grooves milled into the back surface of the plate by means of spot welding. This procedure ensured a good thermal contact between the plate and the thermocouple. The thermocouples were covered with a film of RTV 16 cement in order to insulate them from A.C. noise of the heaters. Each thermocouple lead was brought out through the passages milled into the plate surface to ensure good thermal contact between the heaters and the back surface of the plate.

The water temperature was monitored with three thermocouples placed at different elevations in the water outside of the boundary layer. Thermal stratification caused a variation in the ambient water temperature in the vertical direction, so the bulk water temperature was assumed to be an average of the three values.

The power supply for the heaters was provided by six independently controlled variacs. Figure 4 shows the variac-heater arrangement. With the aid of the strip chart recorder, a constant temperature of the plate

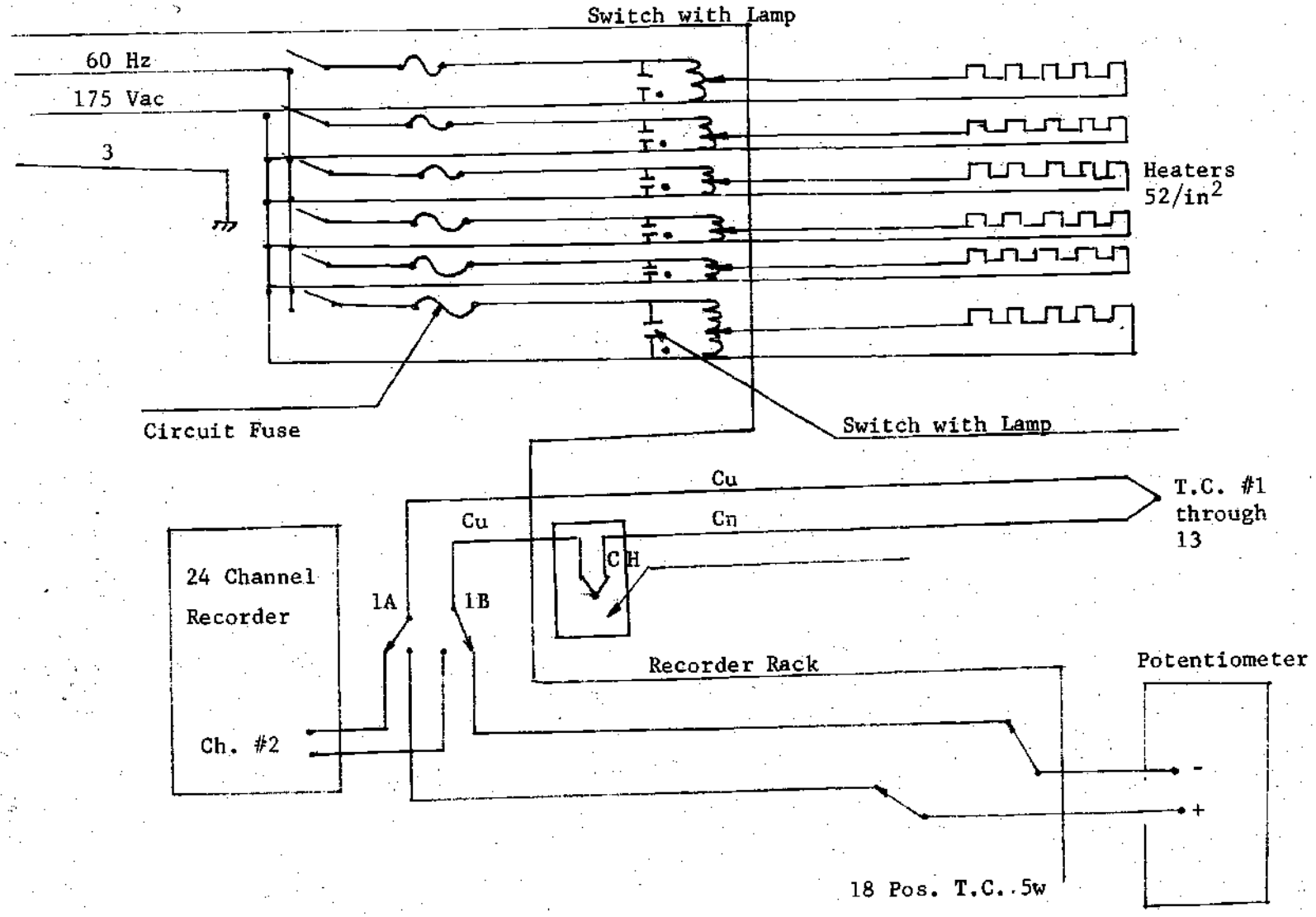

Figure 4. Recorder-Heater Arrangement

was achieved by varying each variac independently.

Differential Interferometer and Camera

There are several optical systems which have been used for the analysis of a temperature field in a transparent medium. Most of them fall into the category of Schlieren, shadowgraph, and interferometric techniques. Although the operation of all three depends upon the variation of the index of refraction, each one is used to measure the different quantities. A quantitative analysis of these systems and their advantages and the disadvantages when applied to the heat transfer measurements are discussed in Appendix B.

A schematic diagram of the differential interferometer is shown in Figure 5. A complete discussion of this interferometer is available in references 14, 16, and 19. A brief summary of its operation follows.

Light rays which leave the mercury discharge light source as shown in Figure 5 are allowed to pass through a filter. The wavelength used in this investigation was 5461 Å. The reason for using this particular wavelength of light was that the relationship between index of refraction and temperature eventually selected was valid only for a wavelength of 5461 Å (21,22).

After leaving the filter, the beam passes through a collecting lens and a polarizer which is oriented so that the light is polarized into two equal magnitude electrical vectors. Both of these components are focused on the first of the three Wollaston prisms, WP1, which causes the rays associated with each component to diverge slightly as they leave the prism. The first Wollaston prism is located at the focal point of the

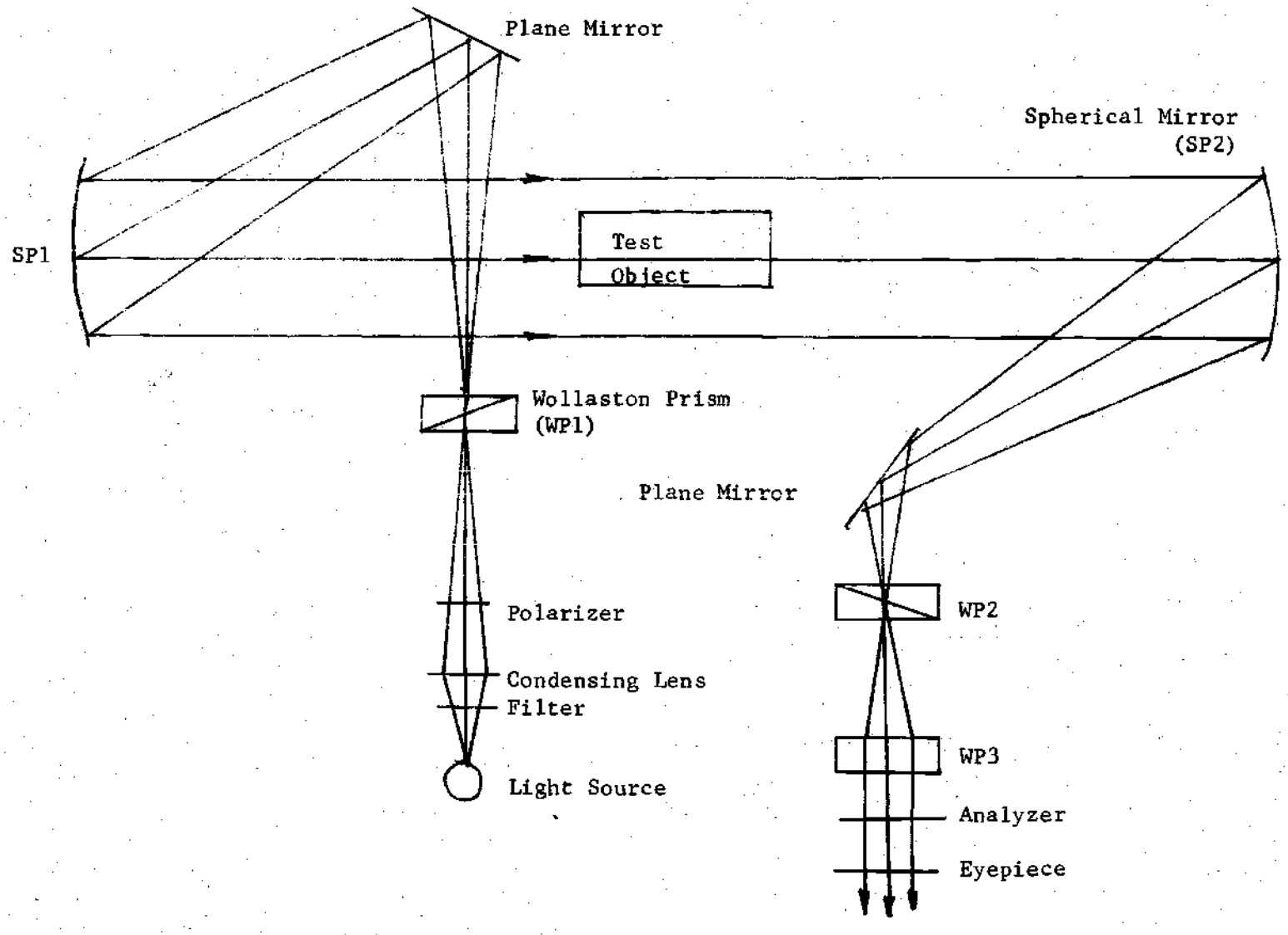

Figure 5. Schematic Diagram of the Differential Interferometer

first spherical mirror. Upon the reflection from the spherical mirror, the two rays travel parallel but slightly separated paths through the test section. After leaving the test section the two rays are focused by the second spherical mirror, SP2, which converges them on the second Wollaston prism, WP2. The second prism is rotated 180 degrees with respect to the first Wollaston prism so that the effect of the first Wollaston prism is reversed. After leaving WP2, the rays pass through WP3, which produces a phase shift between two electric vector components.

The component with the electric vector, E_x, will be referred to as ray x, and the component with the electric vector, E_y, will be referred to as ray y. As discussed above, ray y is deflected upward in the x-z plane and ray x is deflected downward in the x-z plane. The total angle as defined in Figure 6 is given as (24):

$$\alpha = 2(n_e - n_0)\tan\theta_i \tag{2}$$

where $(n_e - n_0)$ is the difference between the extraordinary and the ordinary indices of refraction of the Wollaston prism material, and θ_i is the wedge angle of the Wollaston prism. As the two rays travel parallel but slightly separated paths through the test section, the separation distance, ΔX_s, between ray x and ray y that originally formed an incident ray is

$$\Delta X_s = \alpha g \tag{3}$$

where g is the distance between WP1 and the spherical mirror. By substituting for α, from equation (2), the separation distance can be written as

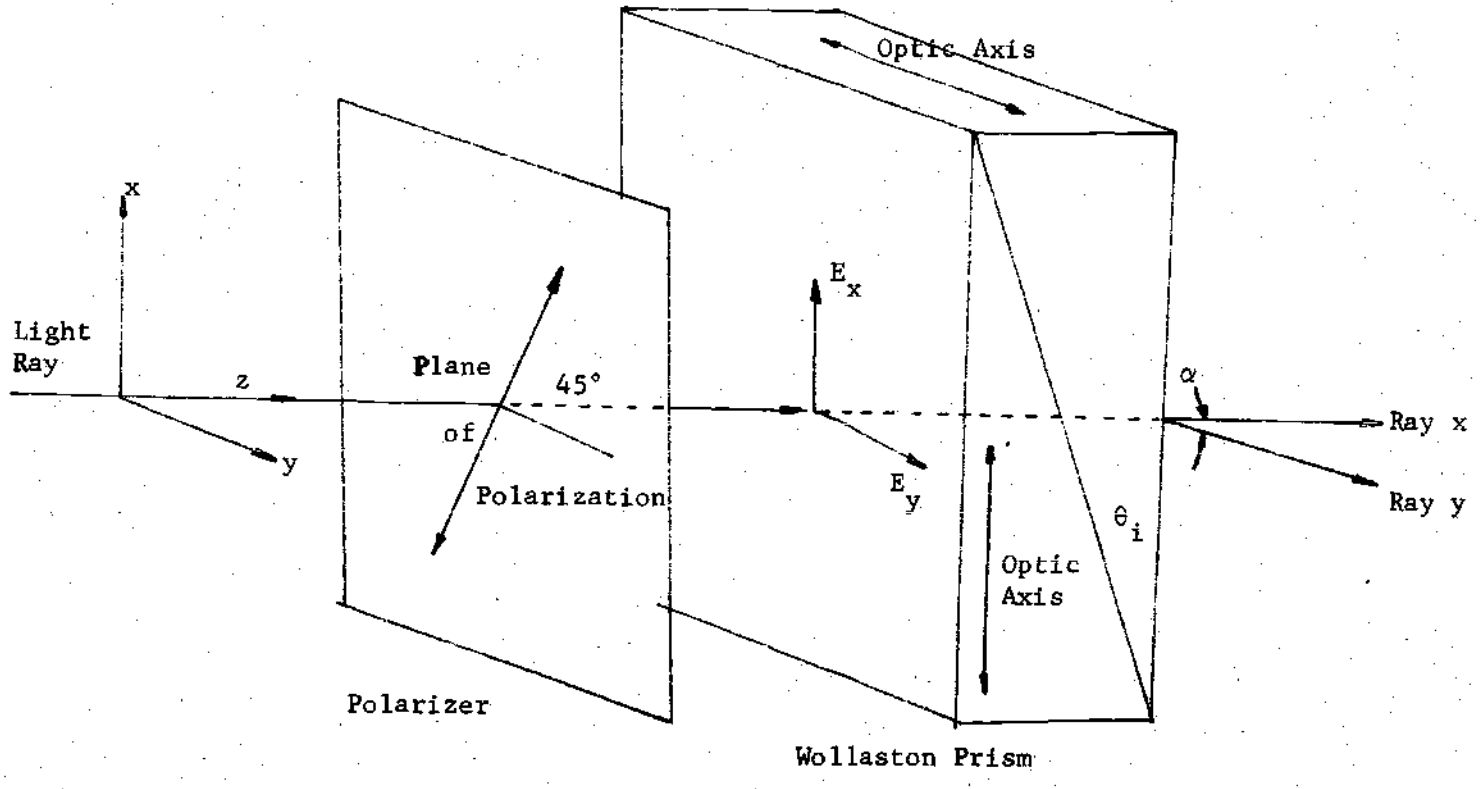

Figure 6. Division of a Single Ray into Two Components

$$\Delta X_s = 2g(n_e - n_0)\tan\theta_i \qquad (4)$$

Upon leaving WP3, the recombined beam passes through the analyzer which produces the interference pattern between two electrical components. The interference pattern which results appears as alternate light and dark bands. This type of pattern is referred to as a parallel fringe pattern. When the third Wollaston prism is removed, the only fringes which appear are those caused by a gradient of index of refraction within the test section. This interference pattern is referred to as an infinite fringe interferogram.

When a heated object is placed in the test section, the two slightly separated rays will experience different optical paths, which result in the parallel fringe interferogram produced by WP3. This deflection of an individual fringe line is proportional to the gradient of the index of refraction. By using Newton's law of cooling, the heat transfer coefficient is derived as (17):

$$h_x = \left[\frac{k_f}{(2Lg\Delta n \tan\theta_i)}\right]\left[\frac{m}{(dn/dT)_w (T_w - T_a)}\right] \qquad (5)$$

In the above equation, dn/dT for water was expressed in the form of a semi-empirical expansion in temperature by Osborn (21) as:

$$dn/dT = -10^{-7}(118.73 + 41.4184T - 0.02376T^2 - 0.0043757T^3) \qquad (6)$$

The above relationship was evaluated for green light having a wavelength of 5461 Å.

Two cameras were used to record the fringe shift photographs. A 4" x 5" still camera was used at all plate positions where laminar flow existed, while a 16 mm motion picture camera was used in the transitional and turbulent regimes. The unsteady nature of the fluid transients caused fluctuations in the fringe pattern in these regimes. The steady state pictures were filmed with a General Precision speed Graflex camera. The film used was Plus-x-ortho Kodak and was exposed for one half second. To record the transient fringe pattern a Bolex H-16 reflex camera was used. The film speed of 18 frames per second with a shutter setting of half open was used. For all the tests a slow speed, Kodak Plus-x film 7276 with an ASA number of 50 was used.

CHAPTER III

EXPERIMENTAL PROCEDURE

There were several preliminary steps that were taken before each test was conducted.

1. The Honeywell strip chart recorder and the millivolt potentiometer were calibrated.

2. The glass panels were cleaned of dust, foreign particles, and any marks.

3. The water tank was filled with distilled water and the water was stirred thoroughly.

4. The plate and the interferometer were aligned by placing two aluminum pieces with identically drilled holes in them on opposite ends of the test tank. When placed in the field of view with the light on, the tank could be rotated until the holes were lined up so that the light rays were parallel to the plate surface.

5. Preliminary runs were made to determine the power input settings for the various heaters, in order to produce a uniform plate temperature.

Upon completion of the above preliminary steps, the heaters were turned on and the power settings were adjusted in order to obtain isothermal conditions. A period of about one to one and one-half hours was required for the plate to stabilize at the desired temperature. However, it was found that the centerline temperature reached nearly a constant

value for a period of about ten minutes, after which it continued to rise slowly. Furthermore, the temperature of the water at the top of the tank rose steadily establishing an increasing vertical temperature gradient in the water due to thermal stratification.

Once it was determined that the plate had stabilized at a desired temperature, the water was stirred thoroughly to reduce the effects of thermal stratification. Interference photographs were taken about five or ten minutes after stirring, which was sufficient time for the random water currents to die down and for the plate to reach a uniform temperature condition once again. The maximum temperature difference between the top and the bottom thermocouples placed in water after the currents had died down was found to be about 2°F. The water temperature was determined by averaging the three thermocouples which were mounted at different elevations.

The plate temperature was determined in the following way. The maximum side to side deviation in the plate temperature at a given elevation was determined to be about 3°F. Since three thermocouples were mounted at one half inch from the leading edge, an average of these three readings was determined. The same spanwise variation in the temperature was assumed to exist at the other three elevation points, where side elevation in the plate temperature was unknown due to availability of only a single centerline thermocouple. For the remaining two elevations where the side deviation was known, an average was determined in each case. By averaging the temperature at each of the six elevation points, an overall average plate temperature was established. A typical temperature distribution at the wall surface is shown in Appendix C. The average plate

temperature evaluated for this test was 81.01°F with a standard deviation of 1.2°F from any point on the plate surface, and 0.76°F from the centerline temperature at any elevation.

Interference photographs were taken with the still camera at vertical positions up to 12 inches from the leading edge. These pictures were spaced from three to four inches apart, and the pictures of both infinite and parallel fringes were taken at each location. Motion pictures were taken for distances greater than 15 inches from the leading edge of the plate. Again, the pictures of both infinite and parallel fringes were taken at each location.

The discussion on the data reduction and the interferogram analysis is presented in Appendix C.

CHAPTER IV

DISCUSSION OF RESULTS

The experimental results are best represented in the form of the tables and graphs. In this chapter the heat-transfer correlations are plotted in terms of familiar non-dimensional parameters and the experimentally obtained values are compared with theoretical values.

The results are subdivided into two main groups. Heat transfer results and flow visualization studies. Furthermore, the steady state heat transfer results are discussed first followed by the results in the transitional regime.

Steady State Heat Transfer

Figure 7 shows representative interferograms of the steady state heat transfer at the different elevations, along the wall. Evaluated values of the heat transfer data from these and others are presented in Figures 8 and 9.

Figure 8 shows the variation of $Nu_x/(Ra_x)^{1/4}$ as a function of the distance from the leading edge. Figure 9 shows the variation of Nu_x as a function of $(Ra_x)^{1/4}$. Both the results are compared with the theoretical results of reference (25). As can be seen, the experimental results compare well with the theory. The discrepancies observed at the low Rayleigh numbers can be attributed to the leading edge effects, and the refraction effects that are discussed in detail later in the section.

Experimental results plotted in Figure 9 are correlated by the

Parallel Fringe Pattern

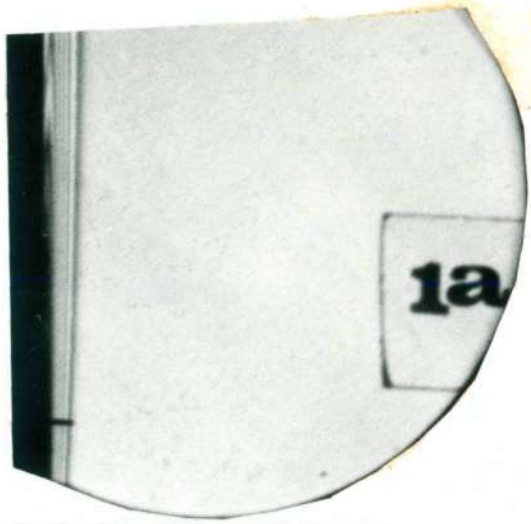

Infinite Frince Pattern

Run 1a $\Delta T = 2.45°F$ (Marker at 1" from Leading Edge)

Parallel Fringe Pattern

Infinite Fringe Pattern

Run 2a $\Delta T = 3.24°F$ (Marker at 4" from Leading Edge)

Figure 7. Interferograms of Steady State Boundary Layer in Water

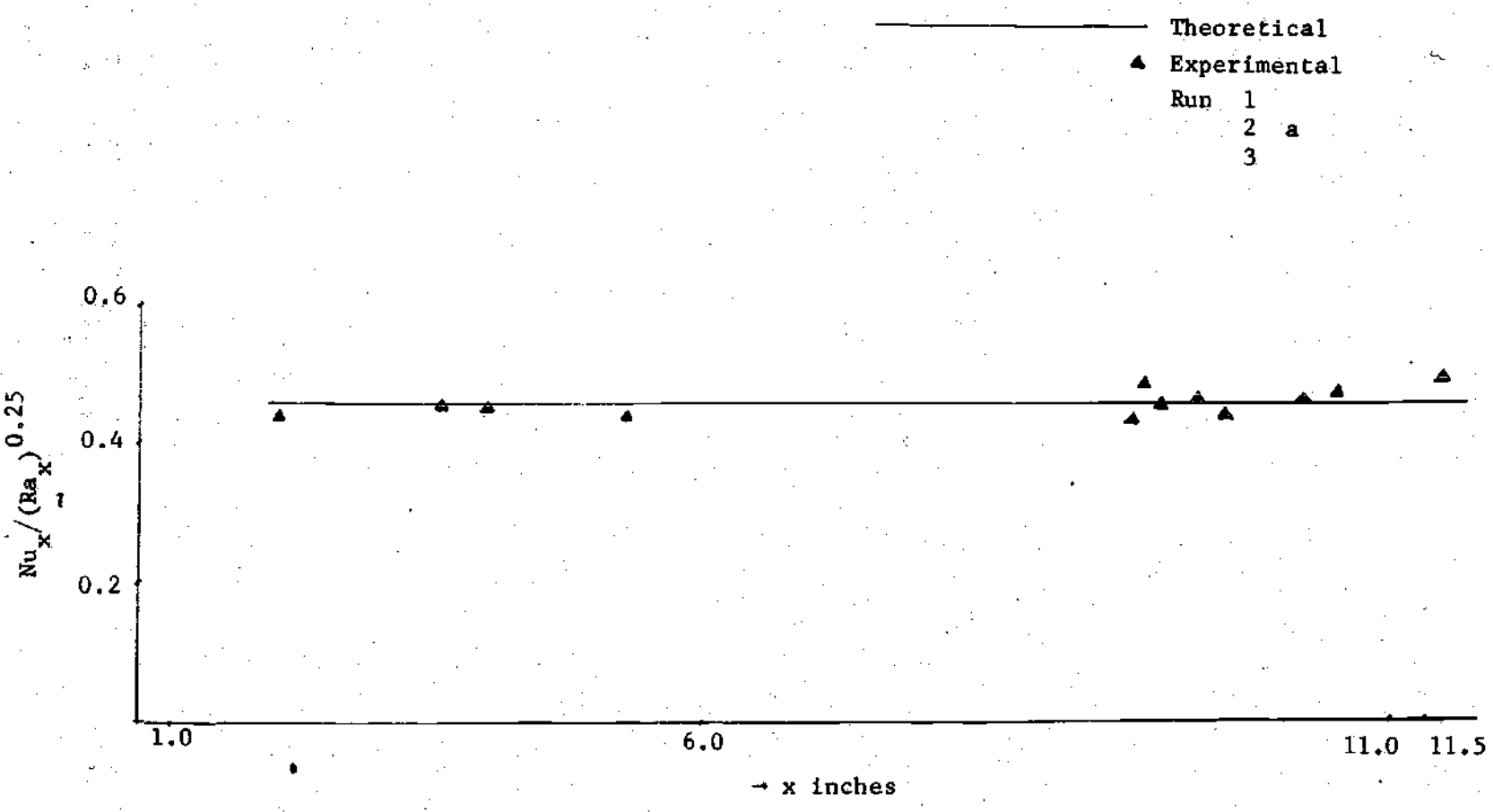

Figure 8. Variation of $Nu_x/(Ra_x)^{0.25}$ with the Distance from Leading Edge

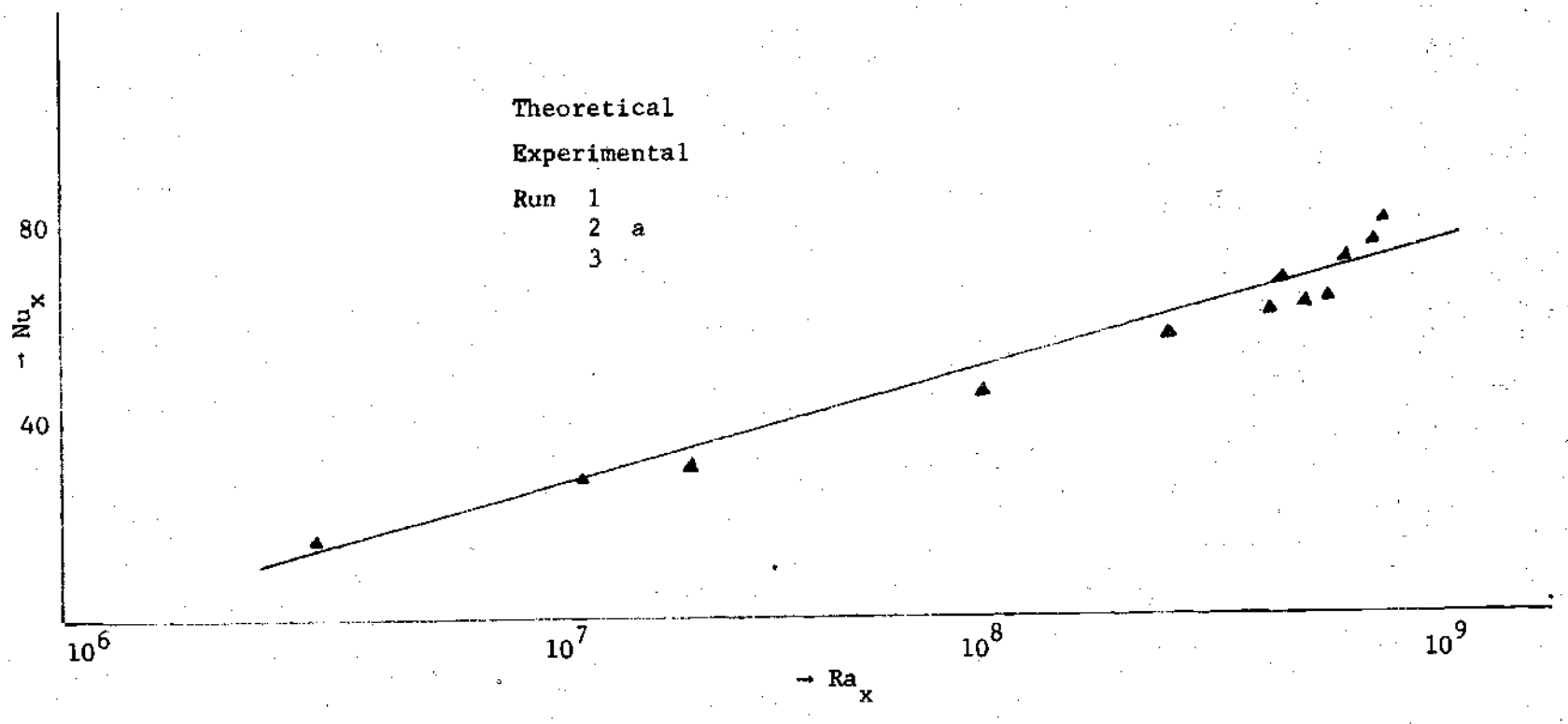

Figure 9. Variation of Nu_x with Local Rayleigh Number for Steady State Runs

following best fit curve,

$$Nu_x = 0.471\ [Gr_x Pr]^{0.25} \qquad (7)$$

The tabulated values of the data can be found in Appendix D. The criteria for the best fit curve are also discussed in Appendix D. The Von Karman-Pohlhausen constant wall temperature analysis of Sparrow (25) results in a heat-transfer correlation

$$Nu_x = 0.508(Pr)^{0.50}\ (0.952 + Pr)^{-0.25}\ (Gr_x)^{0.25}, \qquad (8)$$

which gives a higher coefficient than present water data. The quantity $[0.508(Pr/0.952 + Pr))^{0.25}]$ varies from 0.486 to 0.489 for the Prandtl number variation of 5-6 in the current experiment.

A careful study of the percentage variation of the experimental results [Appendix D] from the theoretical values shows that most of the results, especially those near the leading edge, are lower than the theoretical values. This error could have resulted from refraction effects, which are predominant at higher heat transfer rates.

An experiment was conducted to study the refraction effects under different temperature conditions. A small, carefully machined plexiglass piece was mounted at a location 4" up from the leading edge. The piece was marked with a large arrow and it was located so that the point exactly touched the surface of the heated plate. A series of photographs was taken, such that they represented the infinite fringe patterns of the plate surface under four different temperature conditions. Figure 10a shows the wall with no heat input to the plate. Figures 10b through 10d

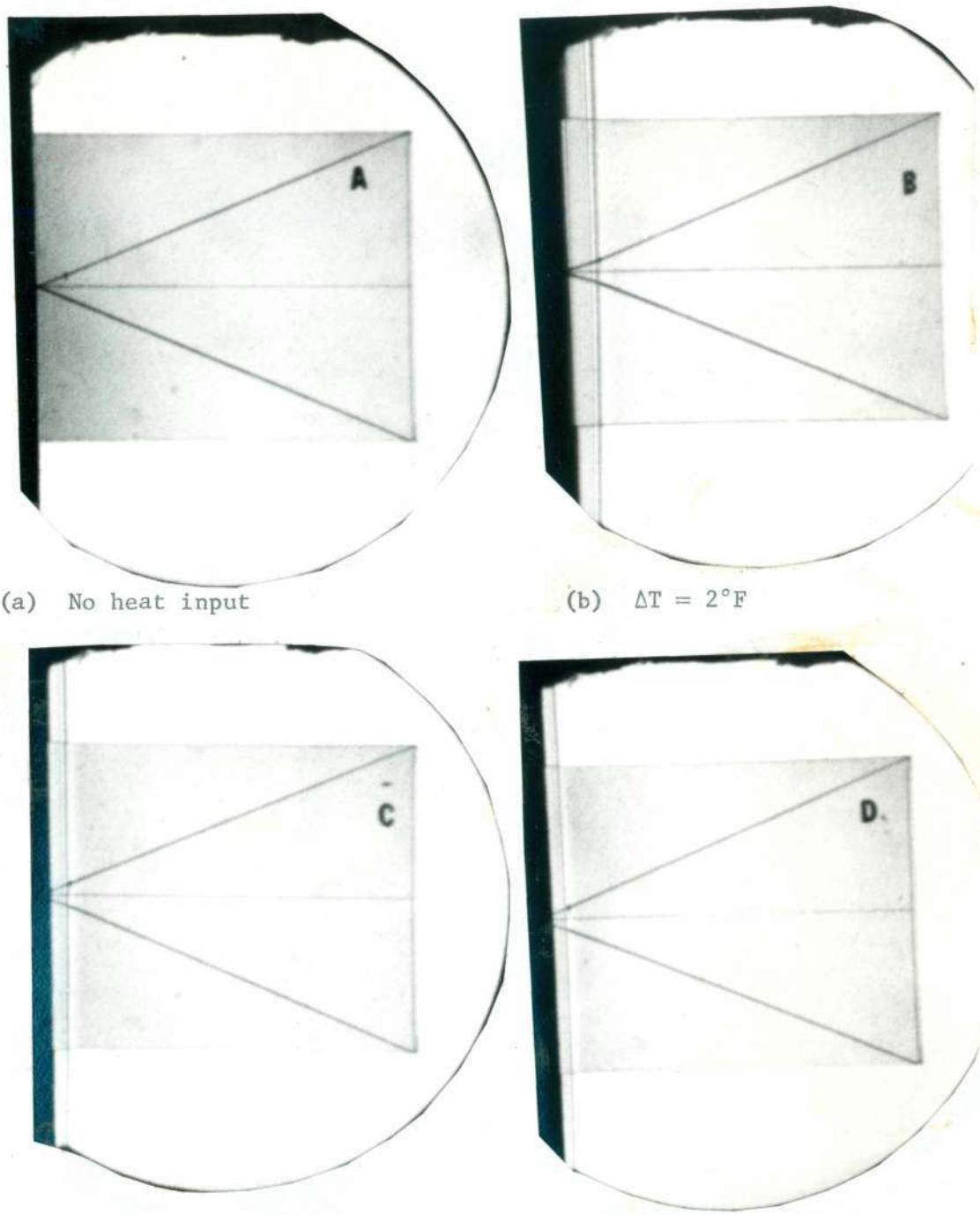

(a) No heat input

(b) $\Delta T = 2°F$

(c) $\Delta T = 4°F$

(d) $\Delta T = 8°F$

Figure 10. The Shift of the Wall due to Refraction

show the plate under the identical conditions except for the wall temperature which was increased to achieve the temperature difference of 2°, 4°, and 8°F, respectively, above the ambient temperature. The apex of the triangle was used as a reference to determine the effects of refraction, as the wall temperature increased. As can be seen, the apex is clearly visible in photograph 10a; however, it is progressively blacked out by a dark region which extends from wall surface at higher temperatures. In the worst case the dark region was about 0.06" while the actual boundary layer thickness was about 0.12". This darkened region led to an error of about 50 percent in the measurement of the boundary layer.

The heat-transfer coefficients were evaluated at higher temperature differences, and a typical set of values is tabulated in Appendix E. However, these values do not reflect the heat transfer coefficients evaluated at the wall, since as discussed above the higher temperature gradients caused the image of the wall to shift considerably into the boundary layer. Referring to the tabulated values of the temperature gradient for an isothermal plate in reference (6), the temperature gradient for the position half way inside the boundary layer was 33 percent of its value at the wall. This explains the large discrepancies observed in the heat transfer measurements at large temperature gradients.

Transient Heat Transfer

Sixteen mm movie film was used to record the interferograms of the local instantaneous heat transfer coefficients in the transitional regime. The local instantaneous values were integrated to obtain the time averaged local heat transfer coefficients.

To achieve a sufficiently high Grashof number such that observations

can be made in the fully turbulent regime, the plate was heated up to 6° to 8°F above the water temperature. However, due to predominant refraction effects at high temperature gradients, the data differed considerably from the theoretical equation (5). A set of typical experimental data can be found in Appendix D. No attempt was made to correlate the local Nusselt number with the local Rayleigh number for these data.

In the transitional regine the local heat transfer coefficient showed significant variation with time. Figure 11 shows a typical plot of the local heat transfer coefficient as a function of time at a location 18 inches from the leading edge. The local value of Grashof number at this point was 1.98×10^8. As can be seen, the heat transfer coefficient varies randomly with an unpredictable cyclic variation.

Flow Visualization Studies

The infinite fringe pattern permits a visual observation of the fluid flow about the heated plate. This simplifies the problem of identifying the type of flow, which exists within the boundary layer. The laminar flow is characterized by a steady nonfluctuating boundary layer, which can be easily differentiated from rapidly oscillating flow which characterizes unsteady, transition, or turbulent flow.

Infinite fringe patterns were studied to determine the critical Rayleigh number which marks the onset of transition, nature of the thermal boundary layers and to determine the frequency of the wave occurrence.

From a study of infinite fringe films, a number of general observations can be made. The boundary layer thickness grew steadily and with the exception of positions far from the leading edge, the double structure of the boundary layer was not evident.

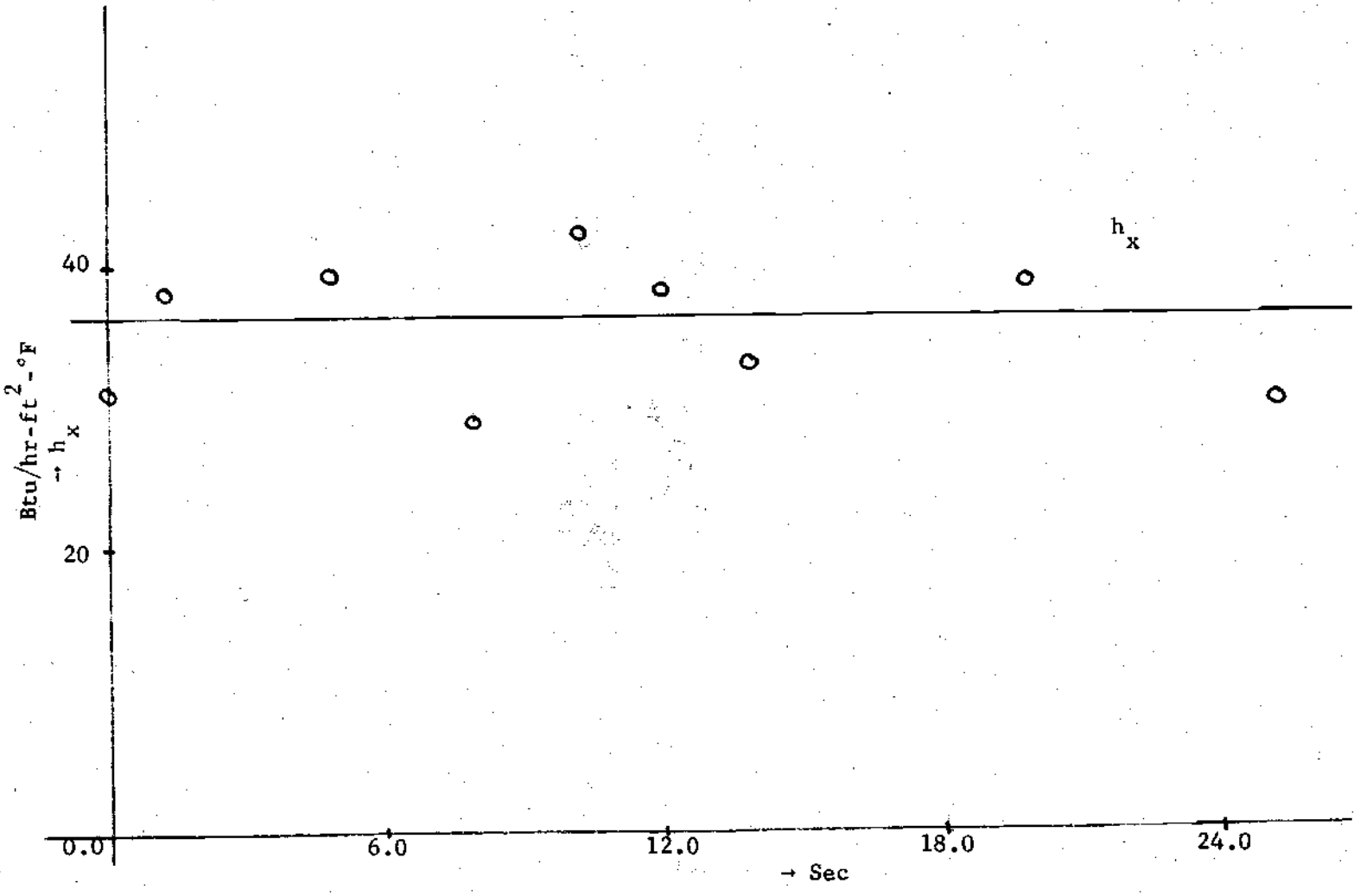

Figure 11. Variation of Local Heat Transfer Coefficient with Time

Up to a height of 8 to 12 inches, the interference lines were steady and gradually increased in thickness, indicating a slow growth of the boundary layer. Beginning at a distance of about 12 inches, waves appeared sporadically which traveled upstream. As shown in Figure 12a, this first appearance of a wave caused only an upward bulging of the outermost fringe lines and no rolling of the lower fringe lines in the thermal sublayer was observed. These waves resemble closely the Tollmien-Schlichting waves and they indicate the beginning of flow instability. The critical Rayleigh number, where the first unsteadyness within the boundary layer appeared was determined from the interferograms as 1.73×10^9. This agrees well with the previous investigations that showed that the transition begins at a Rayleigh number between 2.8×10^8 (27) and 2.0×10^9(4).

The disturbance within the boundary layer which starts out as a single wave increases in duration as it travels downstream by building more waves behind itself. This continues so that at about 18 inches downstream a considerable number of waves arrives before the fluctuations die down. At the same time, the amplitude of the disturbance increases and the rolling up of multiple waves to form a single vortex is observed. Figure 12b shows this process. This type of vortex rolling up was first demonstrated by Eckert and Soehngen (38) for the flow over a flat plate.

As the vortex proceeds downstream, a typical double row vortex system is observed and, as shown in Figure 12c, one vortex near the wall is seen rotating in the clock-wise direction while the fluid in the outer layer is seen rotating in the counter clock-wise direction. The presence of vortices confirms the observation first made by Szewczyk (12) in water.

(a)

First Appearance of a Wave

(b)

Beginning or Roll Up

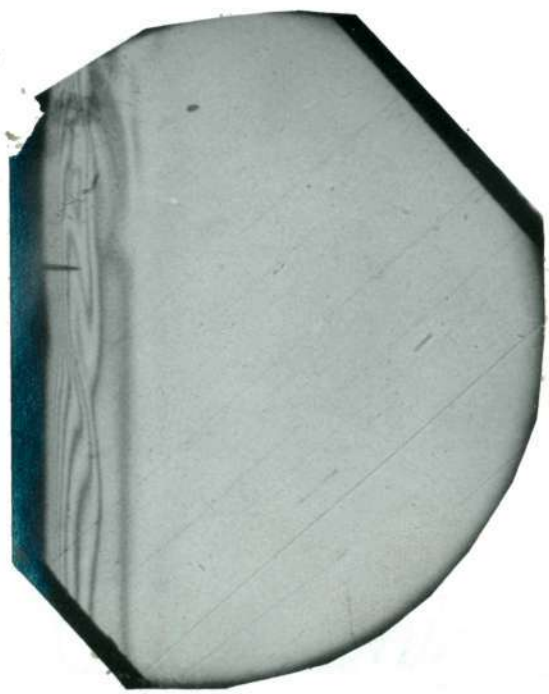

(c)

Vortex Street Layer

(d)

Break Down to Turbulence

Figure 12. Transition of a Laminar Boundary Layer to Turbulent

The smaller and faster vortices near the wall and the larger but much slower vortices in the outer layer may be the result of the decay of two rows of parallel vortices observed by T. Fujii (9) in the "Vortex Street Layer" between the laminar and the transitional flows.

Figure 12d shows the boundary layer for a high wall temperature condition used to achieve higher Grashof number. As can be seen, the outer vortex is very strong and it influences the fluid motion in the inner layer. The inner layer is affected by a large amplification of the disturbance in the outer layer, which overtakes the flow completely and results in the breakdown of the free convection layer from laminar to turbulent. The observation that the inner wave is amplified by highly unstable motion occurring in the outer layer is in agreement with findings of Szewczyk (12). He observed that the described phenomena occur from the strong instability due to inflection point in the velocity profile located outside the maximum velocity. The effect of inflectional stability is to govern the flow which develops into the breakdown of the boundary layer from laminar to turbulent.

The frequency of occurrence of wave as a function of plate position was recorded for the tests conducted in the transitional and turbulent regimes. Unlike similar frequency measurements made in air (14), frequency measurements had to be made over a longer period of time. Furthermore, a quantitative measure of the strength of each wave was recorded by assigning a number from one to five to each wave within five indicating the strongest wave and one the weakest. A typical set of the observations is tabulated in Appendix D. It was observed that a stronger wave was usually followed by a series of weaker waves. As pointed out

before, this behavior leads to a rolling of the waves to form a vortex downstream. Furthermore, unlike air studies the frequency of the occurrence was found to vary for a local value of the Rayleigh number. The frequency of the occurrence of the wave increased steadily over a period of 15 minutes. This could be attributed to a limited bulk volume of water and stratification.

CHAPTER V

ERROR ANALYSIS

The errors encountered in this study are of several types. Significant errors can be attributed to the interferogram not being a true representation of the index of refraction in the boundary layer. These include end effects, refraction errors, and errors due to misalignments and inhomogeneities in the optical systems. Furthermore, errors may also have been caused by nonuniform heating of the plate along the path of the light rays. Errors are also encountered in the readings and calculations from the interferograms including inaccuracy of the fringe positions, and in the case of the Mach-Zehnder interferograms due to improper extrapolation of the temperature profile in the boundary layer. (These errors are discussed in Appendix B.)

A careful attempt was made to align the heated plate in the interferometer test section so as to minimize the alignment errors. Two aluminum sheets with identical holes drilled in them were mounted on each side of the water tank. The light source was turned on and the tank was rotated and leveled until the images of the holes coincided. When the two images overlapped it was assumed that the light rays were parallel to the surface of the heated plate.

Two factors which contribute to the systematic errors often encountered in interferometric measurements are refraction and the end effects. In the following pages, these two errors are treated extensively

and an attempt is made to compare these errors quantitatively for Mach-Zehnder and differential interferometers. The magnitude of these errors has been evaluated considering both air and water as transport media.

End Effect Errors

Theoretically the temperature distribution in the fluid is considered to be two dimensional. Normally the variations in the direction of the light propagation are neglected. However, due to the finite length of the test object, this assumption is not valid. An additional optical path difference between the two separated rays which travel past the test section is introduced at both ends of the test section. The error introduced due to end effects has been analyzed in reference (28), for a single Wollaston prism Schlieren interferometer. This analysis also applies to the differential interferometer. In the section below the end effect error has been evaluated for air and water as transport media.

Differential Interferometer

With reference to Figure 13, the assumptions made in the analysis carried out in reference (28) are:

1. At both the ends of the test section the boundary layer forms a circular arc with its center at the edge of the test section.

2. The temperature distribution in the boundary layer is parabolic or:

$$\frac{T - T_a}{T_w - T_a} = (1 - y/\delta)^2 \qquad (9)$$

where T denotes the local temperature at a distance y perpendicular to the wall.

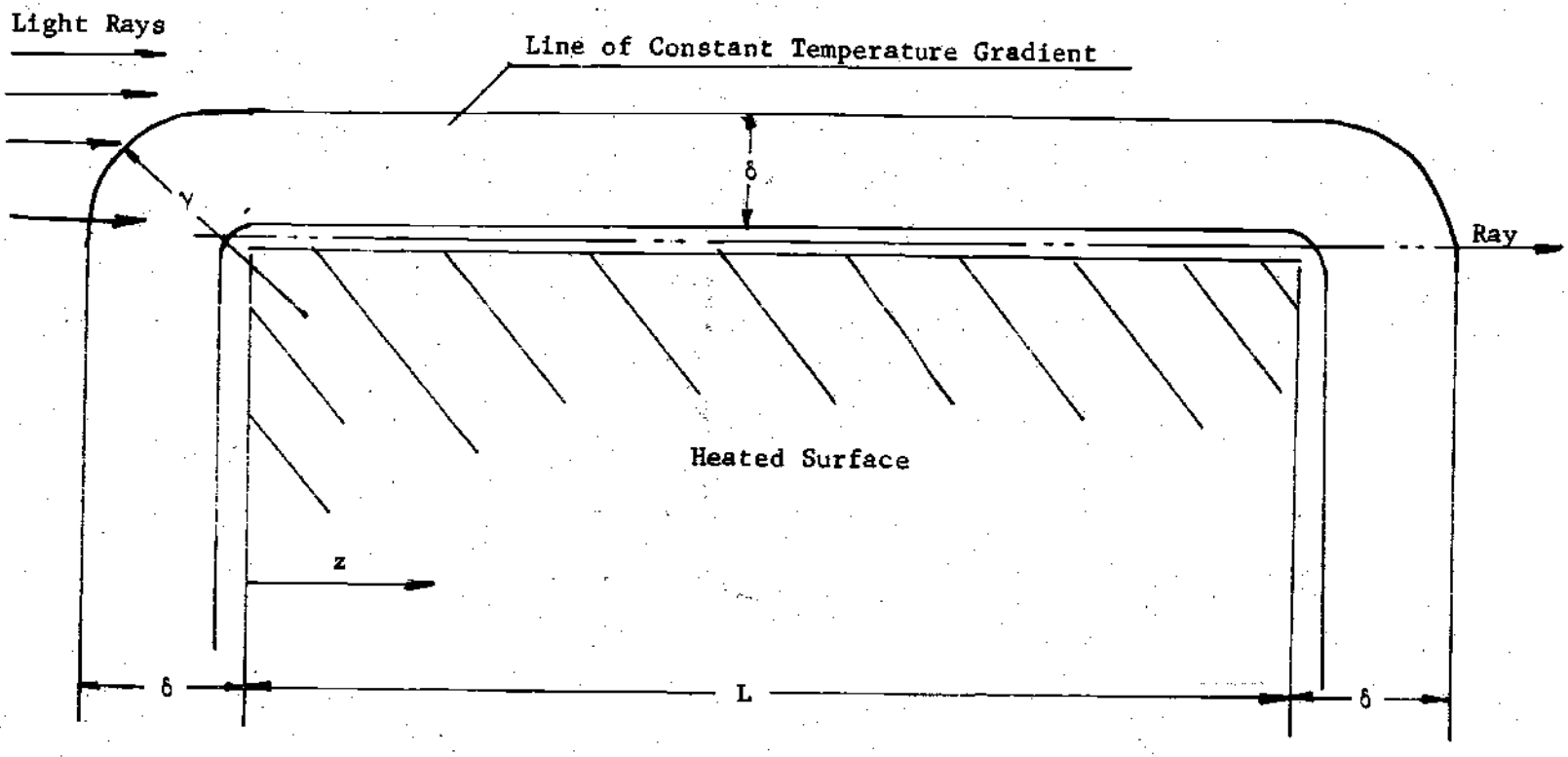

Figure 13. Assumed Temperature Gradient Distribution Used to Determine the End Effect Errors

3. Small temperature difference between the wall temperature and the ambient fluid temperature is assumed such that the index of refraction is given by:

$$n - n_a = \frac{dn}{dT} (T - T_a) \tag{10}$$

With these assumptions, the fraction fringe shift error due to end effect as derived in reference (24) is:

$$e_{end} = \left(2 \frac{\delta}{L}\right) \left(\frac{1}{(\Delta X_s/\delta)(2-\Delta X_s/\delta)}\right) \tag{11}$$

$$\times \left(\frac{(1 - (Sq))}{3} + \frac{(\Delta X_s)^2}{\delta^2} \left(Ln \left(\frac{1 + Sq}{\Delta X_s/\delta}\right) - 2/3(Sq)\right)\right)$$

where

$$Sq = \left(1 - \left(\frac{\Delta X_s}{\delta}\right)^2\right)^{1/2} . \tag{12}$$

ΔX_s is the distance between the two rays traveling through the text section, as defined by equation 4. The values of e_{end} versus $\Delta X_s/\delta$, for several values of δ/L are presented in reference (24). These results are summarized in Table 1 for brevity.

Mach-Zehnder Interferometer

The end effect error for the Mach-Zehnder interferometer has been discussed extensively in reference (29). With the assumption of the identical temperature distribution in the boundary layer,

$$\frac{T - T_a}{T_w - T_a} = (1 - y/\delta)^2 \tag{9}$$

the end error derived in reference (29) is,

$$e_{end} \approx 2/3 \frac{\delta}{L} \tag{13}$$

A tabulated value of end effect error is presented in Table 2 as a function of δ/L.

Table 1. End Effect Error as a Function of $\Delta X_s/\delta$ and δ/L for Air and Water

$\frac{\Delta X_s}{\delta}$	e_{end} (percent)					
	δ/L					
	0.005	0.010	0.015	0.020	0.025	0.03
0.05	0.081	0.163	0.245	0.327	0.408	0.490
0.10	0.131	0.262	0.394	0.525	0.657	0.788
0.15	0.169	0.339	0.509	0.678	0.848	1.018
0.20	0.200	0.401	0.602	0.803	1.004	1.205
0.25	0.226	0.453	0.680	0.907	1.133	1.360

Table 2. End Effect Error as a Function of δ/L for the Mach-Zehnder Interferometer

e_{end} (%)	δ/L					
	0.005	0.010	0.015	0.020	0.025	0.03
	0.333	0.667	1.000	1.333	1.667	2.00

Comparing Tables 1 and 2, the following conclusions can be drawn.

1. In the case of the differential interferometer, the end effect error is a function of ray separation.

2. Considering the identical ratio of the boundary layer thickness to the width of the test section, it can be seen that the end effect error

is larger for the Mach-Zehnder interferometer than for the differential interferometer.

3. The error, as calculated for the Mach-Zehnder and the differential interferometer, is always positive. That is, the temperature or a temperature gradient larger than the true values would be indicated if no corrections were applied. For the differential interferometer this results in a higher value of the heat transfer coefficient at the wall than the correct value.

4. In the case of the differential interferometer, an error in the fringe shift measurement leads to an error in the heat transfer measurement. However, in the case of the Mach-Zehnder interferometer, an error in the fringe shift is related to an error in the temperature measurement. From the error in the temperature as a function of the distance from the plate, the error in $(q/A)_{conv} = - k(d\theta/dy)_{y=0}$ needs to be calculated. A detailed discussion on this calculation can be found in reference (10). In an experimental study, Goldstein (10) determined that the maximum end effect error for water resulted in a heat transfer coefficient measurement that was off by as much as 1.6 percent. This error is greater than the end effect error present in a differential interferometer for the predicted prism angles and the test section size.

5. For the present investigation, the maximum end effect error in heat transfer measurement was found to be 0.2 percent. This error value is based on a Wollaston prism angle of one degree, a test section width of five inches, and a maximum boundary layer thickness of 0.54 inch. The boundary layer thickness value was typical for water with a Rayleigh number of 3.44×10^8.

Refraction Error

Another important error encountered in the interferometric systems is the refraction error. The gradient of the density, and therefore the gradient of refractive index normal to the light ray, may be large enough to produce an appreciable curving or refraction of the light rays. As a result, the temperature or the temperature gradient distribution evaluated from the interferograms on the assumption of unrefracted light rays may lead to an error.

The refraction error has been treated quite extensively in reference (30) for the Mach-Zehnder interferometer. With reference to Figure 14, the assumptions made in this reference are:

1. The index of refraction is assumed to be constant in the direction of the travel of the light ray.

2. The index of refraction can be expressed by a power series.

With reference to Figure 14, the index of refraction is,

$$n/n_a = 1 + b_1 W_w + b_2 W_w^2 + b_3 W_w^3 + \ldots \qquad (14)$$

where W_w is the distance measured perpendicular to the plate and represents the locus of the refracted light ray in the medium. W_w can be expressed in terms of the coordinate along the width of the plate as

$$W_w = a_0 + a_1 z + a_2 z^2 + \ldots \qquad (15)$$

Here a_1, a_2, b_1, and b_2 are arbitrary constants.

With the above assumptions, the change in the optical path of the

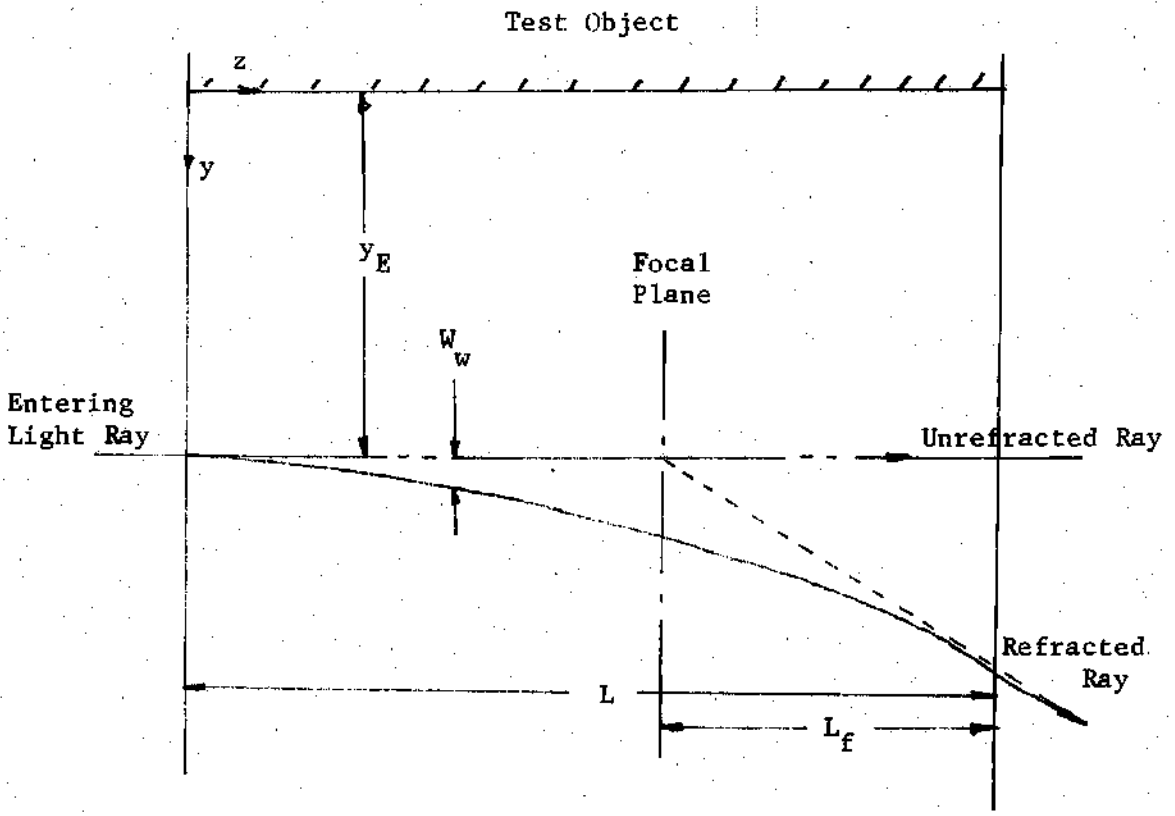

Figure 14. Schematic Diagram of a Refracted Ray

light ray passing through the medium due to refraction is (30),

$$\Delta L_{ref} = b_1^2 L^3 \left\{\left(\frac{\alpha_w}{2} - \frac{1}{6}\right) + L^2 b_2 (-\alpha_w^2 + \alpha_w - 1/5)\right. \tag{16}$$

$$+ L^4 \left[b_2^2 (-2/3\ \alpha_w^2 + 4/9\ \alpha_w - 4/63)\right.$$

$$\left.\left. + b_1 b_3 (\alpha_w^3 - 3/2\ \alpha_w^2 + 3/4\ \alpha_w - 3/28)\right]\right\}$$

where

$$\alpha_w = L_f/L \tag{16a}$$

and

$$b_0 = 0, \qquad b_1 = 1/n_0 \left[\frac{\partial n}{\partial W_w}\right]_{W_w=0}$$

$$b_2 = \frac{1}{2n_0} \left[\frac{\partial^2 n}{\partial W_w^2}\right]_{W_w=0}, \qquad b_3 = \frac{1}{6n_0} \left[\frac{\partial^3 n}{\partial W_w^3}\right]_{W_w=0}. \tag{16b}$$

L_f is the distance of the focal plane from the end nearest to the camera and L is the width of the test section.

Differential Interferometer

In the case of the differential interferometer, the interferogram results from the interference between two rays, one which travels along the surface of the heated plate, and the other displaced by a distance equal to the separation distance from the surface of the wall. Each ray is independently affected by refraction which produces an independent change in the optical path length. Since dark interference fringes are obtained due to destructive interference between these two rays, the

effective change in the optical path length due to refraction will be,

$$\Delta l_{ref} = \Delta L_{ref/y=0} - \Delta L_{ref/y=\Delta X_s} \tag{17}$$

and the nondimensional refraction error will be,

$$e_{ref} = \frac{\Delta L_{ref/y=0} - \Delta L_{ref/y=\Delta X_s}}{(n_{y=0} - n_{y=\Delta X_s})L} \tag{18}$$

Combining equations 16 through 18, two separate formulas have been derived for the refraction error when the light ray passes through air and water.

Refraction Error, Air. When the light rays pass through air, the index of refraction can be related to temperature by the Dale-Gladstone relationship. Accordingly,

$$n = 1 + k/T, \tag{19}$$

which leads to

$$\frac{1}{n_{y=0} - n_{y=\Delta X_s}} = \frac{1}{k}\left(\frac{T_w\, T_{\Delta X_s}}{T_{\Delta X} - T_w}\right) \cdots \tag{20}$$

Combining equations 16 through 20, the error due to refraction would be,

$$\begin{aligned} e_{ref.} = \left[\frac{1}{k} \cdot \frac{T_\omega\, T_{\Delta x_s}}{T_{\Delta x_s} - T_\omega}\right]\Big\{ & F(\alpha_\omega)\left(\frac{L}{\delta}\right)^2\left[(\delta b_{1\omega})^2 - (\delta b_{1\Delta x_s})^2\right] \\ & + G(\alpha_\omega)\left(\frac{L}{\delta}\right)^4\left[(\delta b_{1\omega})^2(\delta^2 b_{2\omega}) - (\delta b_{1\Delta x_s})^2(\delta^2 b_{2\Delta x_s})\right] \\ & + H(\alpha_\omega)\left(\frac{L}{\delta}\right)^6\left[(\delta b_{1\omega})^2(\delta^2 b_{2\omega})^2 - (\delta b_{1\Delta x_s})^2(\delta^2 b_{2\Delta x_s})^2\right] \\ & + I(\alpha_\omega)(L/\delta)^6\left[(\delta b_{1\omega})^3(\delta^3 b_{3\omega}) - (\delta b_{1\Delta x_s})^3(\delta^3 b_{3\Delta x_s})\right]\Big\} \end{aligned} \tag{21}$$

where, $F(\alpha_\omega) = \left(\frac{\alpha_\omega}{2} - 1/6\right)$ (21a)

$G(\alpha_\omega) = \left(-\alpha_\omega^2 + \alpha_\omega - 1/5\right)$ (21b)

$H(\alpha_\omega) = \left(-2/3\,\alpha_\omega^2 + 4/9\,\alpha_\omega - 4/63\right)$ (21c)

$I(\alpha_\omega) = \left(\alpha_\omega^3 - 3/2\,\alpha_\omega^2 + 3/2\,\alpha_\omega - 3/28\right)$ (21d)

For the present analysis, a simple parabolic temperature profile in the boundary layer was assumed. Again, combining equations 9 and 16, one can show that:

$$\frac{T - T_a}{T_w - T_a} = (1 - y/\delta)^2 \tag{9}$$

and,

$$\delta b_{1\omega} = \left[\frac{-2k}{na}\right]\left[\frac{1}{T_\omega}\right]\left[\frac{T_\omega - T_a}{T_\omega}\right] \tag{22a}$$

$$\delta^2 b_{2\omega} = \left[\frac{-4k}{na}\right]\left[\frac{1}{T_\omega}\right]\left[\frac{T_\omega - T_a}{T_\omega}\right]^2 + \frac{1}{na}\left[\frac{k}{T_\omega}\right]\left[\frac{T_\omega - T_a}{T_\omega}\right] \tag{22b}$$

$$\delta^3 b_{3\omega} = \left[\frac{-8k}{na}\right]\left[\frac{1}{T_\omega}\right]\left[\frac{T_\omega - T_a}{T_\omega}\right]^3 + \left[\frac{4k}{na}\right]\left[\frac{1}{T_\omega}\right]\left[\frac{T_\omega - T_a}{T_\omega}\right]^2 \tag{22c}$$

and

$$\delta b_{1\Delta x_s} = \left[\frac{-2k}{na}\right]\left[\frac{1}{T_{\Delta x_s}}\right]\left[\frac{T_\omega - T_a}{T_{\Delta x_s}}\right]\left[1 - \frac{\Delta x_s}{\delta}\right] \tag{23a}$$

$$\delta^2 b_{2\Delta x_s} = \left\{\left[\frac{-4k}{na}\right]\left[\frac{1}{T_{\Delta x_s}}\right]\left[\frac{T_\omega - T_a}{T_{\Delta x_s}}\right]^2\left[1 - \frac{\Delta x_s}{\delta}\right]^2 + \left[\frac{4k}{na}\right]\left[\frac{T_\omega - T_a}{T_{\Delta x_s}}\right]^2\right\} \tag{23b}$$

$$\delta^3 b_{3\Delta x_s} = \left\{\left[\frac{-8k}{na}\right]\left[\frac{1}{T_{\Delta x_s}}\right]\left[\frac{T_\omega - T_a}{T_{\Delta x_s}}\right]^3\left[1 - \frac{\Delta x_s}{\delta}\right]^3 + \left[\frac{4}{na}\right]\left[\frac{k}{T_{\Delta x_s}}\right]\left[\frac{T_\omega - T_a}{T_{\Delta x_s}}\right]^2\left[1 - \frac{\Delta x_s}{\delta}\right]^2\right\} \tag{23c}$$

Equations 22 and 23 can be substituted into equation 21 to give a final expression for the refraction error as a function of the dimensionless parameters, $\Delta X_s/\delta$, δ/L, and α_w. These errors are tabulated in Table 3. Figure 15 shows these errors plotted as a function of the above dimensionless parameters.

Refraction Error, Water. When the light ray passes through water it experiences an appreciable curving due to large variations in the refractive index with temperature. The index of refraction has been related to temperature differences by Tilton and Taylor (23) in a relationship such as

$$n = 1.33446615 - \frac{6.3669(T-20)^3 + 2364.81(T-20)^2 + 76.735.3(T-20)}{(T+65.7081) \times 10^7} \tag{24}$$

Combining equation 24 with equations 17 through 23, the error due to refraction would be

Table 3. Refraction Error for Differential Interferometer Applied to Air (Percentage Error x 10^2; $\Delta X_s/\delta = 0.005$)

δ/L	α_w	$\phi = \frac{T_w - T_a}{T_w}$		
		0.05	0.10	0.20
0.10	0.00	0.209	0.126	0.087
	0.25	0.0525	0.0316	0.0215
	0.333	≃ 0.00	≃ 0.00	≃ 0.00
	0.50	- 0.150	- 0.0633	- 0.0433
	0.667	- 0.221	- 0.126	- 0.0858
	1.00	- 0.420	- 0.253	- 0.168
0.20	0.00	0.0525	0.0316	0.0215
	0.25	0.0131	0.00795	0.00535
	0.333	≃ 0.00	≃ 0.00	≃ 0.00
	0.50	- 0.0262	- 0.0158	- 0.0107
	0.667	- 0.0525	- 0.0316	- 0.0214
	1.00	- 0.105	- 0.0632	- 0.0426
0.50	0.00	0.00841	0.0056	0.0034
	0.25	0.0021	0.00126	0.00085
	0.333	≃ 0.00	≃ 0.00	≃ 0.00
	0.50	- 0.0042	0.00253	0.00171
	0.667	- 0.0084	0.00506	0.00342
	1.00	- 0.0168	0.01012	0.00689

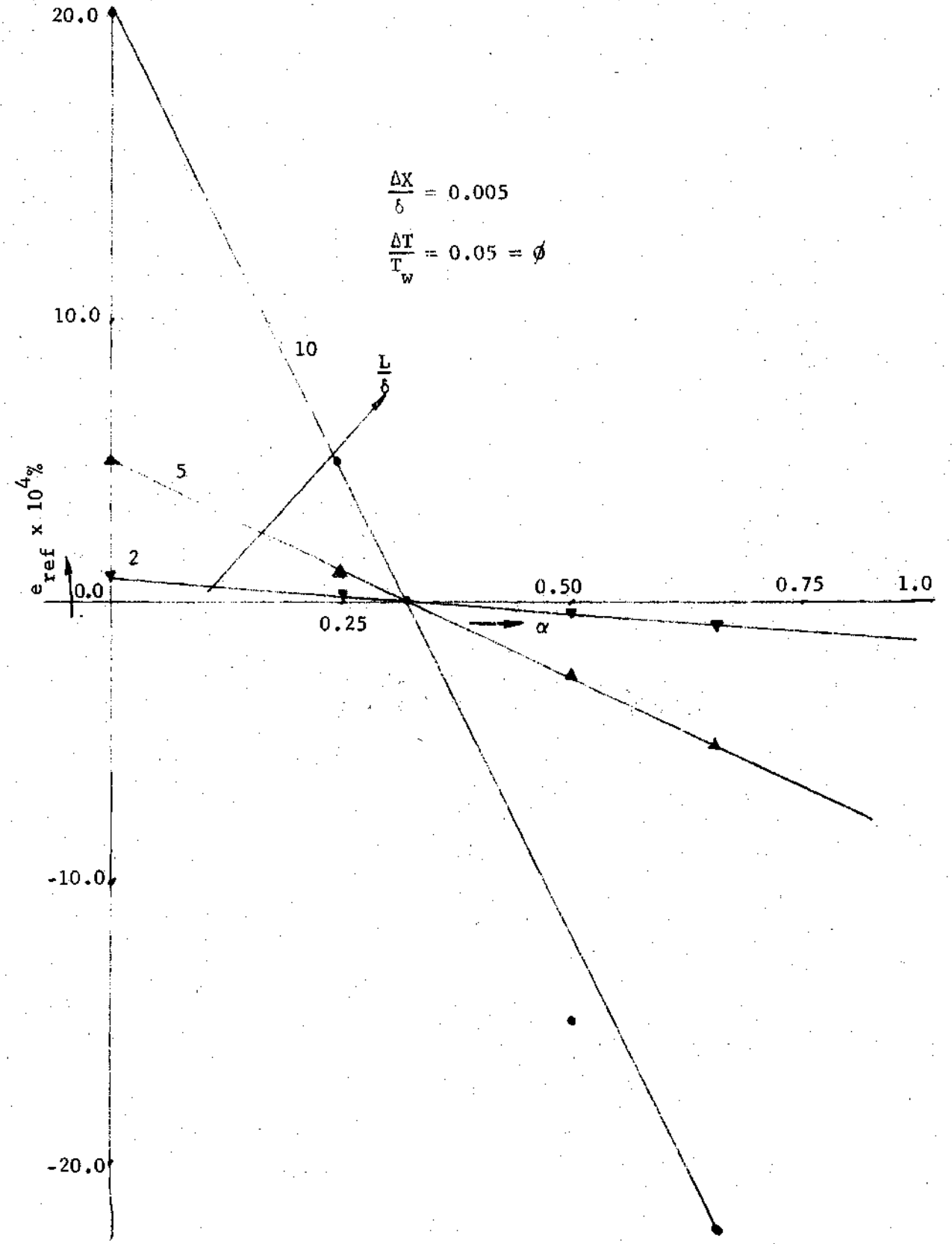

Figure 15. Refraction Error for Differential-Air System

$$e_{ref.} = \left[\frac{1}{n_{y=0} - n_{y=\Delta X_s}}\right] \left\{ F(\alpha\omega)\left(\frac{L}{\delta}\right)^2 \left[(\delta b_{1\omega})^2 - (\delta b_{1\Delta X_s})^2\right] \right.$$
$$+ G(\alpha\omega)\left(\frac{L}{\delta}\right)^4 \left[(\delta b_{1\omega})^2(\delta^2 b_{2\omega}) - (\delta b_{1\Delta X_s})^2(\delta^2 b_{2\Delta X_s})\right] \quad (25)$$
$$+ H(\alpha\omega)\left(\frac{L}{\delta}\right)^6 \left[(\delta b_{1\omega})^2(\delta^2 b_{2\omega})^2 - (\delta b_{1\Delta X_s})^2(\delta^2 b_{2\Delta X_s})^2\right]$$
$$\left. + I(\alpha\omega)\left(\frac{L}{\delta}\right)^6 \left[(\delta b_{1\omega})^3(\delta^3 b_{3\omega}) - (\delta b_{1\Delta X_s})^3(\delta^3 b_{3\Delta X_s})\right] \right\}$$

For the present analysis, a simple parabolic profile as given by equation 9 was assumed. The refraction errors as a function of $\Delta X_s/\delta$, δ/L, and α_w are tabulated in Table 4. These errors are also plotted as a function of the above nondimensional parameters in Figure 16.

Mach-Zehnder Interferometer

Refraction effects for the Mach Zehnder interferometer have been considered by Eckert and Soehngen (31), by Howes and Buchele (32), and by Goldstein (10). In general the effects of the higher order terms in the governing equation were neglected in the analyses. In the present analysis, the effect of those higher order terms is included.

In the case of the Mach-Zehnder interferometer, the refraction error is given by

$$e_{ref} = \frac{L_{ref}}{\Delta n \cdot L} \quad (26)$$

where L_{ref} is given by equation 16. Combining equations 16, 20, and 24 gives two separate formulae for air and for water as the transport media.

Refraction Error, Air. Combining equations 16, 20, and 22, the refraction error formula for air can be shown to be

Table 4. Refraction Error for Differential Interferometer Applied to Water ($\Delta X_s/\delta = 0.005$, Percent Error)

δ/L	α_w	$\phi = \frac{T_w - T_a}{T_w}$		
		0.05	0.10	0.20
0.10	0.00	1.10	2.204	4.08
	0.25	0.282	0.715	1.634
	0.333	0.0042	0.0048	1.2303
	0.50	- 0.560	- 1.130	- 1.236
	0.667	- 1.134	- 2.75	- 3.913
	1.00	- 2.301	- 5.310	-28.04
0.20	0.00	0.292	0.699	1.299
	0.25	0.071	0.179	0.373
	0.333	0.0232	0.0218	0.0234
	0.50	- 0.141	- 0.355	- 0.710
	0.667	- 0.284	- 0.716	- 1.45
	1.00	- 0.571	- 1.14	- 2.845
0.50	0.00	0.045	0.114	0.237
	0.25	0.013	0.028	0.0597
	0.333	$\simeq$ 0.00	$\simeq$ 0.00	$\simeq$ 0.00
	0.50	- 0.023	- 0.057	- 0.119
	0.667	- 0.095	- 0.115	- 0.238
	1.00	- 0.091	- 0.230	- 0.478

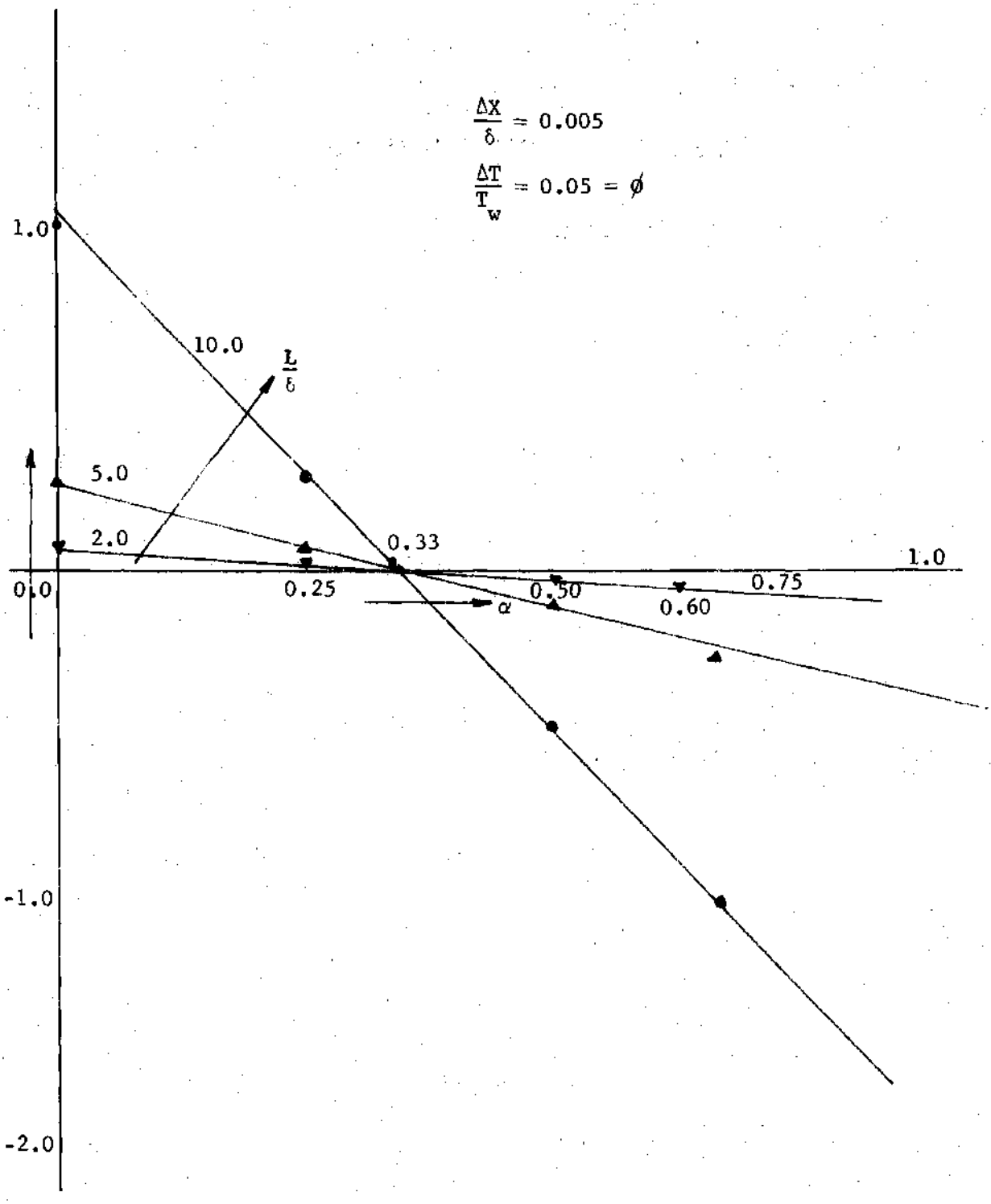

Figure 16. Refraction Error for Differential-Water System

$$e_{ref.} = \left[\frac{T_a}{k}\right]\left[\frac{T}{T_a - T}\right]\left[\left(\frac{L}{\delta}\right)^2(\delta b_1)^2 F(\alpha_\omega) + \left(\frac{L}{\delta}\right)^4(\delta b_1)^2 \times (\delta^2 b_2)(G(\alpha_\omega)) + \left(\frac{L}{\delta}\right)^6\left\{(\delta b_1)^2(\delta^2 b_2)^2 H(\alpha_\omega) + (\delta b_1)^3(\delta^3 b_3) I(\alpha_\omega)\right\}\right] \quad (27)$$

where the terms in the brackets are identified by equations 22a through 22c.

The tabulated values of the refraction errors as a function of dimensionless parameters, y/δ, δ/L, and α_w are given in Table 5. Figure 17 shows these errors as a function of y/δ and α_w for a typical value of y/δ observed in air.

Refraction Error, Water. The refraction error for water was obtained by combining equations 16, 22, and 24.

$$e_{ref.} = \left[\frac{1}{n - n_a}\right]\left\{\left(\frac{L}{\delta}\right)^2(\delta b_1)^2 F(\alpha_\omega) + G(\alpha_\omega)\left(\frac{L}{\delta}\right)^4(\delta b_1)^2(\delta^2 b_2) + \left(\frac{L}{\delta}\right)^6\left[(\delta b_1)^2(\delta^2 b_2)^2 H(\alpha_\omega) + (\delta b_1)^3(\delta^3 b_3) I(\alpha_\omega)\right]\right\} \quad (28)$$

The terms in the brackets are identified by equations 22a through 22c.

The tabulated values of the refraction error for this system are listed in Table 6 as a function of the nondimensional parameters, y/δ, δ/L, and α_w. Figure 18 shows these values plotted as a function of the above parameters for a typical value of y/δ.

Since the primary objective of the present analysis was to compare the refraction errors involved in the differential interferometer and the Mach-Zehnder interferometer, the tabulated values are used for the comparison. Tables 7 through 10 show the refraction errors involved in the

Table 5. Refraction Error for Mach-Zehnder Interferometer Applied to Air (Percent Error, $y/\delta = 0.005$)

δ/L	α_w	$\phi = \frac{T_w - T_a}{T_w}$		
		0.05	0.10	0.20
0.10	0.00	0.244	0.185	0.331
	0.25	0.0613	0.0415	0.083
	0.333	$\simeq$ 0.000	$\simeq$ 0.000	$\simeq$ 0.000
	0.50	- 0.122	- 0.093	- 0.166
	0.667	- 0.245	- 0.186	- 0.332
	1.00	- 0.491	- 0.373	- 0.647
0.20	0.00	0.0613	0.0465	0.383
	0.25	0.0153	0.0116	0.002
	0.333	$\simeq$ 0.00	$\simeq$ 0.00	$\simeq$ 0.00
	0.50	- 0.0306	- 0.0232	- 0.041
	0.667	- 0.0613	- 0.0415	- 0.083
	1.00	- 0.122	- 0.0393	- 0.166
0.50	0.00	0.00981	0.00745	0.0132
	0.25	0.00245	0.00186	0.0033
	0.333	$\simeq$ 0.00	$\simeq$ 0.00	$\simeq$ 0.00
	0.50	- 0.0049	- 0.0037	- 0.0066
	0.667	- 0.0093	- 0.00745	- 0.0132
	1.00	- 0.0196	- 0.0149	- 0.0265

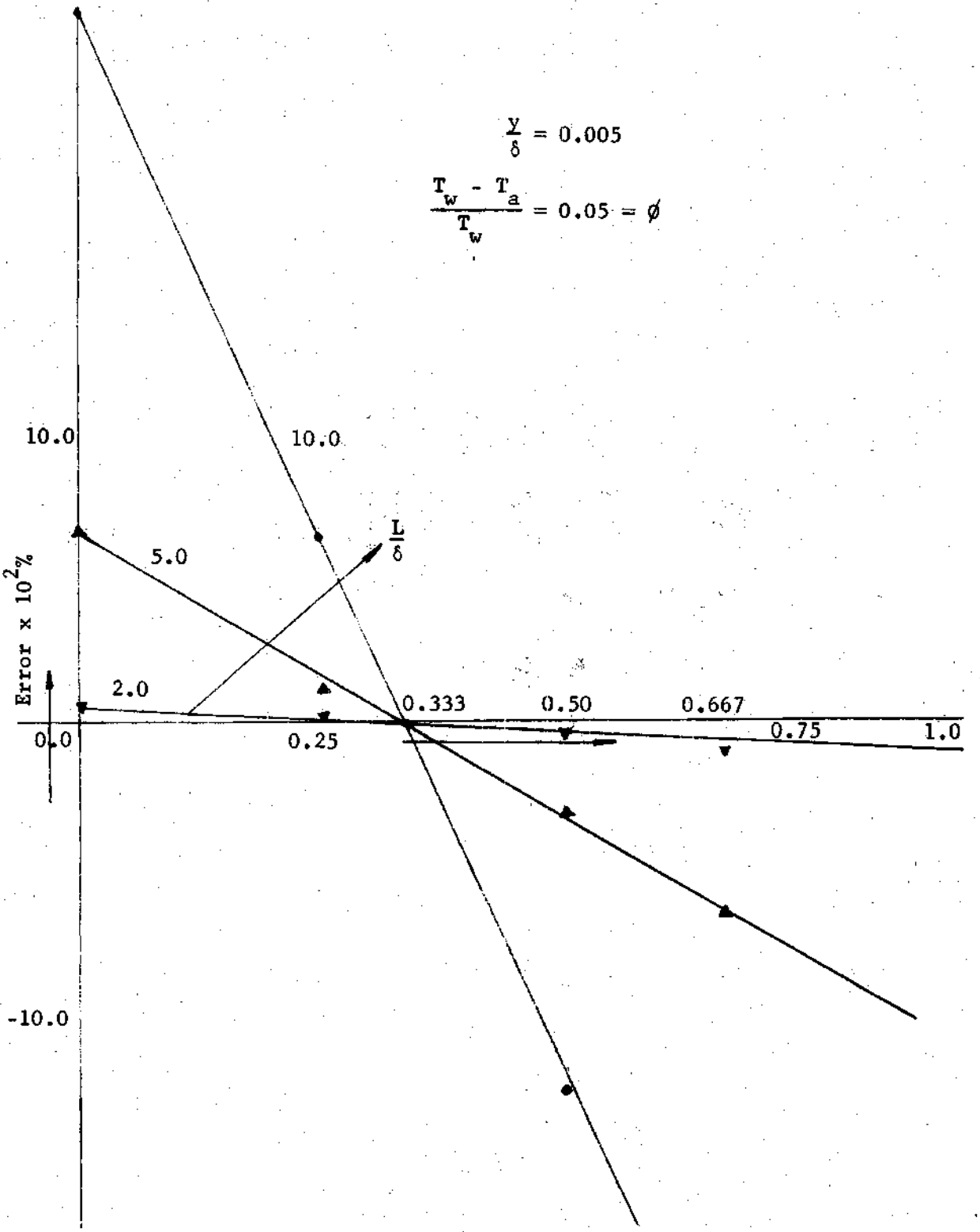

Figure 17. Refraction Error for Mach-Zehnder-Air System

Table 6. Refraction Error for Mach-Zehnder Interoferometer Applied to Water

δ/L	α_w	$\phi = \frac{T_w - T_a}{T_w}$		
		0.05	0.10	0.20
0.10	0.00	1.280	5.41	19.32
	0.25	0.336	1.430	5.034
	0.333	0.040	0.0486	0.
	0.50	- 0.648	- 2.81	-10.09
	0.667	- 1.310	- 5.78	-22.75
	1.00	- 2.667	-12.07	-48.94
0.20	0.00	0.326	1.430	5.62
	0.25	0.082	0.363	1.45
	0.333	$\simeq$ 0.00	0.0030	0.025
	0.50	- 0.164	- 0.724	- 2.871
	0.667	- 0.328	- 1.460	- 5.83
	1.00	- 0.66	- 2.95	-11.92
0.50	0.00	0.052	0.233	0.931
	0.25	0.013	0.058	0.234
	0.333	$\simeq$ 0.00	$\simeq$ 0.00	$\simeq$ 0.00
	0.50	- 0.026	- 0.116	- 0.467
	0.667	- 0.052	- 0.233	- 0.936
	1.00	- 0.105	- 0.468	- 1.

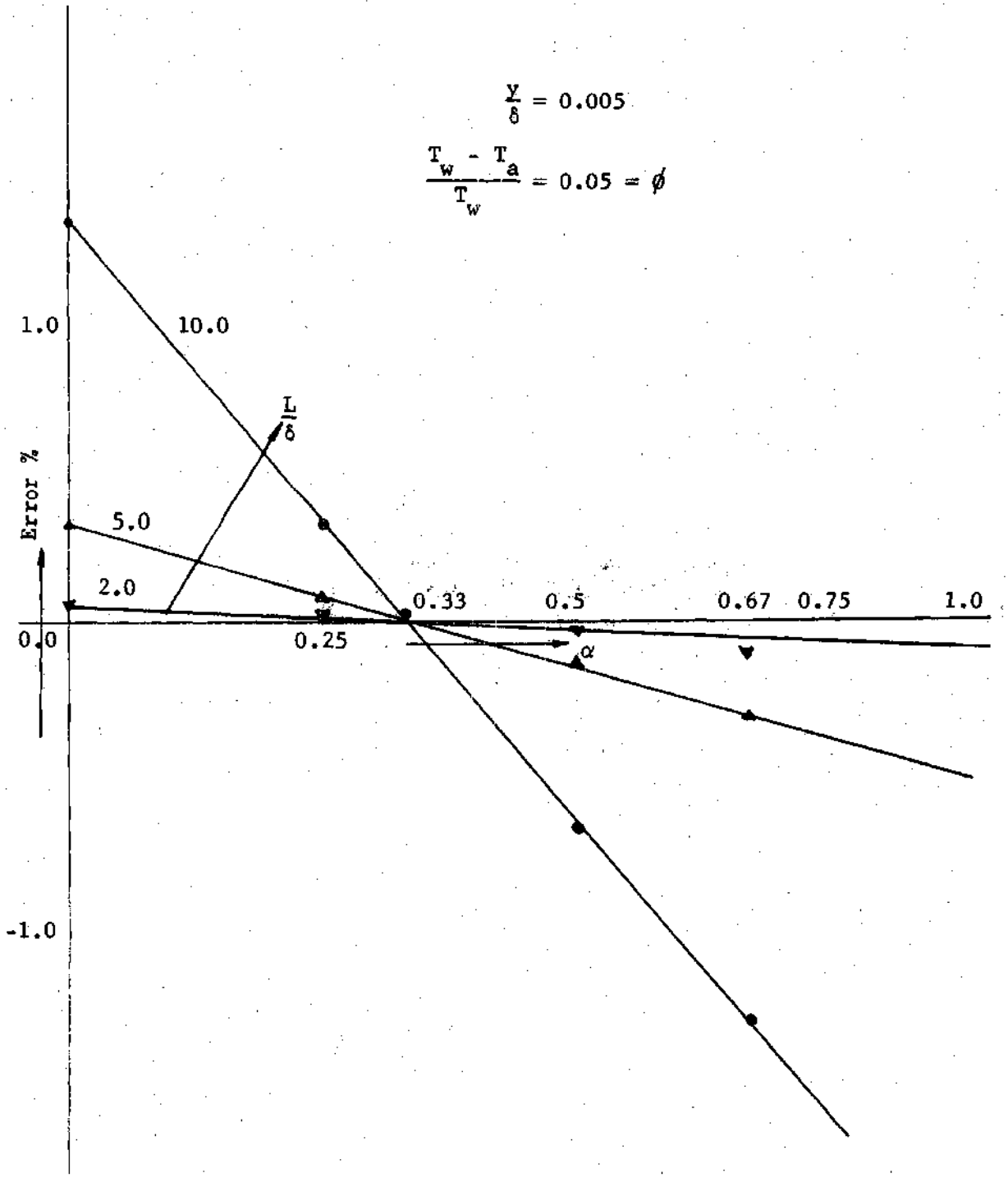

Figure 18. Refraction Error for Mach-Zehnder-Water System

Table 7. Refraction Error as a Function of y/δ, for Mach-Zehnder Interferometer Applied to Air

y/δ	0.005	0.010	0.05	0.10	0.7	1.0
$e_{ref} \times 10^2$ (%)	1.5	1.5	1.4	1.2	0.10	0.00

Table 8. Refraction Error as a Function of $\Delta X_s/\delta$, for Differential Interferometer Applied to Air

$\Delta X_s/\delta$	0.005	0.010	0.05	0.10	0.75	1.0
$e_{ref} \times 10^2$ (%)	0.013	0.026	0.14	0.31	2.3	0.077

Table 9. Refraction Error as a Function of y/δ for Mach-Zehnder Interferometer Applied to Water

y/δ	0.005	0.010	0.05	0.10	0.75	1.0
e_{ref} (%)	0.082	0.0813	0.075	0.068	0.005	0.00

Table 10. Refraction Error as a Function of $\Delta X_s/\delta$ for Differential Interferometer Applied to Water

$\Delta X_s/\delta$	0.005	0.010	0.05	0.10	0.75	1.0
e_{ref} (%)	0.071	0.071	0.07	0.07	0.068	0.068

fringe measurements. These errors are tabulated for the identical temperature and geometrical conditions which existed in the current study.

The above analysis leads to the following conclusions.

1. Even though the higher order terms involving α_w are considered, the refraction error is minimum at $\alpha_w = 1/3$ for all four cases. This confirms Wachtell's observation for the first approximation for $\alpha_w = 1/3$ that in the first approximation evaluation of an interferogram focused one-third the way in from the exit window will give the true density or temperature distribution even though refraction is not taken into account.

2. The refraction error increases rapidly with increase in the ratio L/δ, or for the lower values of δ. This agrees well with the condition set by Wachtell that the dimensionless quantity $C = (L/\delta)(k(\rho-\rho_0))^{0.5}$ should be less than 0.70 for the refraction formula to be valid.

3. This report is in agreement with the conclusion of Wachtell (30), who reported minimum error at $\alpha_w = 1/3$. Considering the second and higher order approximations, the error involved in the measured temperature gradient distribution is minimum and less than about 0.05 percent if the interferogram is focused at one-third the way in from the exit window.

4. For the thin boundary layer such as existed in the water studies, it was found that the refraction error is sometimes as large as 1,000 times as large as existed in air studies. This results in an appreciable error in the temperature or the temperature gradient measurement made in the liquid media.

5. Tables 7 and 8 depict the percentage refraction errors involved in the evaluation of the differential interferograms and the Mach-Zehnder interferograms, respectively. For the quantitative comparison, it was assumed that both interferograms were photographed for the identical boundary layers in air. As is evident, the percentage error in the fringe measurement is higher for the Mach-Zehnder interferometer than the percentage error involved in the differential interferometer. However, in the case of the Mach-Zehnder interferometer, the error is much less at the points away from the surface wall (given by higher values of y/δ), and the error reaches zero at $y/\delta = 1.0$. It should be noted that most of the temperature or the temperature gradient measurements are taken at points near the surface wall.

6. In the case of the water studies, as depicted in Tables 9 and 10, the same trend is observed for the refraction errors. However, the difference between the error involved in the differential interferometer and the Mach-Zehnder interferometer is not as much as that in the case of the air studies.

7. In the case of the differential interferometer, an error in the fringe shift itself leads to an error in the heat transfer measurements. However, in the case of the Mach-Zehnder interferometer, an error

in the fringe shift is related to an error in the temperature measurements. From the error in the temperature, the error in the heat transfer parameter needs to be calculated. A detailed discussion of these calculations can be found in reference (10). Goldstein calculated the refraction error for the extreme case to be 0.5 percent for his experimental study. These results were based on the assumption that the interferograms were focused at one third from the exit window.

8. For the present investigation, the maximum refraction error in the heat transfer measurements for the extreme case of a very thin boundary layer ($L/\delta = 10.0$), and for a Wollaston prism angle of one degree, was calculated to be 0.025 percent. The above calculation is based on the assumption that the interferograms were focused at the location, one third from the exit window.

9. It should be noted that the refraction error mentioned in Chapter IV is not the same error evaluated here. In the present analysis, it is assumed that under the influence of refraction, the light ray passing along the surface was traveling along a different curved path and introduced the error in the fringe shift. The error referred to in Chapter IV, on the other hand, was caused by bending or refraction of the light rays away from the heated surface leaving a black region next to the surface where no information on the temperature gradient can be obtained.

CHAPTER VI

CONCLUSIONS

The differential interferometer provides an excellent means of flow visualization in liquids. It is also a reasonably good device for the measurement of heat transfer coefficients at low temperature gradients in liquids. At higher temperature gradients the accurate measurement of heat transfer coefficients becomes complicated due to refraction effects.

The flow visualization study of the flow structure in the transitional regime shows that a double row vortex system arises and the outer layer controls the development of flow and impresses its effects onto more stable inner layers close to the wall. The frequency of occurrence of the thermal wave was found to be unstable. The frequency increased gradually over a longer period of time resulting in a continuous burst of waves.

An error analysis which considered end effect and refraction errors showed that the differential interferometer was capable of measuring the heat transfer coefficient more accurately than the Mach-Zehnder interferometer. For the differential interferometer, all measurements were made at the heated surface. Therefore, a shift in the image of the wall into the boundary layer due to refraction can limit the applicability of the differential interferometer when measurements are made in liquids. However, the differential interferometer provides an excellent means of measuring heat transfer rates.

CHAPTER VII

RECOMMENDATIONS

The technique of segmented heaters worked well to achieve isothermal conditions along the plate. However, the spanwise temperature variation was considerable; therefore, segmented heaters could be used across the plate width to achieve a more uniform temperature condition.

The differential interferometer research should be extended to study in detail the formation of vortices in the free convection transitional and turbulent boundary layers. Such studies could bring new insight to a peculiar phenomenon and aid in the extension of current theories on free convection at high Rayleigh numbers.

The refraction error evaluated analytically during the present investigation should be verified experimentally as a function of various parameters.

APPENDICES

APPENDIX A

PROPERTY VALUES

The physical properties of the aluminum plate were used for preliminary design calculations, and very accurate values were not necessary. The values of thermal and electrical conductivities and specific heat were obtained from reference (33).

The properties of water were much more important in calculating the final results. The values of density, dynamic viscosity, and specific heat for water were obtained from reference (34). The values of the thermal conductivity of water in the range of interest did not vary appreciably. Linearly interpolated values were used from reference (34).

The values for the refractive index of water as a function of temperature were obtained from reference (21). The equation used was semi-empirical and valid for the entire range of temperatures at a wavelength of 5461 Å. The governing equation is

$$dn/dT = - 10^{-7} (118.73 + 41.4184T - 0.02376T^2 - 0.0043757T^3) \qquad (6)$$

Tilton and Taylor (22) obtained values of the index of refraction for water experimentally and interpolated the complete set of values over the temperature range of 0°C to 25°C by the equation

$$n = 1.33446615 - \frac{6.3669(T-20)^3 + 2364.81(T-20)^2 + 76.735.3(T-20)}{(T+65.7081) \times 10^7} \quad (24)$$

Comparing the values obtained from equation 24 with those obtained by Osborn (21), it was found that the values of Tilton and Taylor are slightly higher. This was attributed to the fact that the values defined by Tilton and Taylor are the ratio of the velocity of light in air to the velocity of light in water both being at the same temperature rather than Osborn's ratio of the velocity of light in vacuum to the velocity of light in water.

Throughout this investigation equation 6 was used for the index of refraction in water, since it directly gives the value of the temperature gradient which is of importance here.

There are two references (35,36) which discuss the reference temperature to be used in order to evaluate nondimensional parameters for heat transfer calculations in air. However, for water it is not evident what, if any, reference temperature should be used. Since throughout the present investigation the maximum temperature difference between the plate and the free stream was only 8°F, it seemed quite reasonable to evaluate all of the properties at the averaged film temperature, $T_f = (T_w + T_a)/2$.

It was calculated that, at the bottom of the tank, the maximum water gauge pressure was about 0.15 atm. Since the effect of pressure variation on the index of refraction at pressures less than one atmosphere is negligible (37), the pressure effects were neglected.

APPENDIX B

QUANTITATIVE COMPARISON OF VARIOUS OPTICAL SYSTEMS

There are several optical systems which have been used for the measurement of temperature distribution in a transparent medium. Most of them fall into the broad category of Schlieren, shadowgraph, and the interferometric techniques. Although all of them depend on variation of index of refraction in the medium to produce an interference pattern, quite different quantities are measured in each one. Shadowgraph systems measure the variation of the second derivative of the index of refraction. Schlieren, as well as the differential interferometer, measures the first derivative of the index of refraction. Mach-Zehnder interferometers permit the direct measurement of the change in the refractive index, and as a result they give the information on the temperature distribution directly.

Optical measurement of the temperature field has many advantages over other temperature measuring devices. The most important one is the absence of an instrument probe which could influence the temperature field.

The following section evaluates the sensitivity of each device in terms of various nondimensional parameters.

Schlieren Systems

To study the Schlieren systems, the path of a light beam in a medium whose index of refraction is a function of position must be analyzed. Considering Figure 19, the relative intensity or contrast is (29),

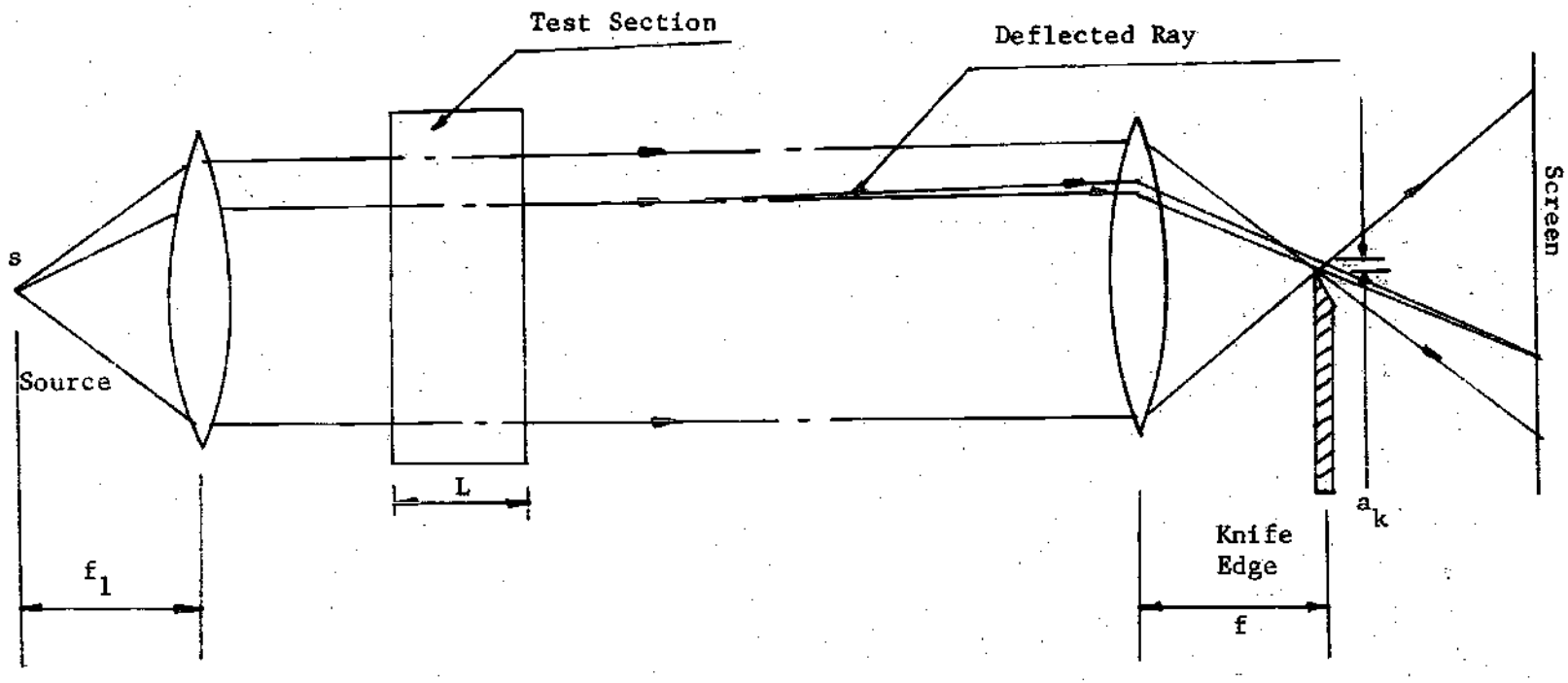

Figure 19. A Typical Schlieren System

$$\frac{\Delta I}{I_0} = \pm \frac{f_2}{a_k n_a} L \left[\frac{\partial n}{\partial y}\right] \tag{29}$$

For gas as a transport medium,

$$\frac{\partial n}{\partial y} = - \frac{k}{T} \frac{\partial T}{\partial y} \tag{30}$$

$$\frac{\Delta I}{I_0} = \mp \frac{f_2}{a_k n_a} L \left[\frac{k}{T^2} \frac{\partial T}{\partial y}\right] \tag{31}$$

To evaluate the contrast quantitatively, the following typical values for the parameters of the system were assumed:

$f_2 = 3.28$ ft

$L = 0.328$ ft

$a_k = 3.28 \times 10^{-3}$ ft

For convenience, a parabolic profile for the temperature distribution was assumed. The profile is given by equation 9.

For water as a transport medium, equation 32 modified to,

$$\frac{\Delta I}{I_0} = \pm \frac{f_2}{a_k n_a} L \left[\frac{\partial n}{\partial T} \frac{\partial T}{\partial y}\right] \tag{32}$$

Tables 11 and 12 show the contrast as a function of y/s and L/s_x when measurements are made in air and water, respectively.

Table 11. Relative Contrast, $\Delta I/I_0$, for Schlieren System with Measurement in Air

L/δ	y/δ	$\phi = \frac{T_w - T_a}{T_w}$		
		0.05	0.10	0.20
10.0	0.005	3.89	3.11	6.25
	0.01	3.87	3.10	6.24
	0.05	3.75	3.03	6.18
	0.10	3.58	2.92	6.08
	0.75	1.07	0.95	2.36
	1.00	0.00	0.00	0.00
5.0	0.005	1.94	1.55	3.12
	0.010	1.93	1.55	3.12
	0.050	1.87	1.51	3.09
	0.10	1.79	1.46	3.00
	0.75	0.53	0.47	1.18
	1.00	0.00	0.00	0.00
2.0	0.00	0.77	0.62	1.25
	0.01	0.77	0.62	1.24
	0.05	0.75	0.60	1.23
	0.10	0.71	0.58	1.21
	0.75	0.21	0.19	0.47
	1.00	0.00	0.00	0.00

Table 12. Relative Contrast, $\Delta I/I_0$, for Schlieren System with Measurement in Water

L/δ	y/δ	$\phi = \frac{T_w - T_a}{T_w}$		
		0.05	0.10	0.20
10.0	0.005	4.34	11.8	23.6
	0.01	4.32	11.7	23.4
	0.05	4.13	11.2	22.4
	0.10	3.91	10.63	21.16
	0.75	1.06	2.88	5.50
	1.00	0.00	0.00	0.00
5.0	0.005	2.17	5.90	11.8
	0.01	2.16	5.87	11.73
	0.05	2.06	5.62	11.22
	0.10	1.95	5.31	10.58
	0.75	0.53	1.44	2.75
	1.00	0.00	0.00	0.00
2.0	0.005	0.86	2.36	4.72
	0.01	0.86	2.34	4.69
	0.05	0.82	2.24	4.48
	0.10	0.78	2.12	4.23
	0.75	0.21	0.57	1.10
	1.00	0.00	0.00	0.00

Shadowgraph Systems

In the shadowgraph system, the linear displacement of the perturbed light is measured rather than the angular deflection as in the Schlieren systems. With reference to Figure 20, the relative contrast can be expressed as (29):

$$\frac{\Delta I}{I_o} = -\frac{SL}{n_a}\frac{\partial^2 n}{\partial y^2} \tag{33}$$

For Air

$$\frac{\Delta I}{I_o} = -\frac{SL}{n_a}\left[\frac{2k}{T^3}\left(\frac{\partial T}{\partial y}\right)^2 - \frac{k}{T^2}\frac{\partial^2 T}{\partial y^2}\right] \tag{33a}$$

For Water

$$\frac{\Delta I}{I_o} = -\frac{SL}{n_a}\left[\frac{\partial}{\partial y}\left(\frac{\partial n}{\partial T}\right)\left(\frac{\partial T}{\partial y}\right)\right] \tag{33b}$$

To evaluate the contrast quantitatively, the following typical parameters were assumed: S = 100L and L = 0.328 ft.

For convenience, a parabolic profile for the temperature distribution in the boundary layer was assumed.

$$\frac{T - T_a}{T_w - T_a} = (1 - y/\delta)^2 \tag{9}$$

Tables 13 and 14 show the contrast as a function of θ and y/δ for air and water as transport media.

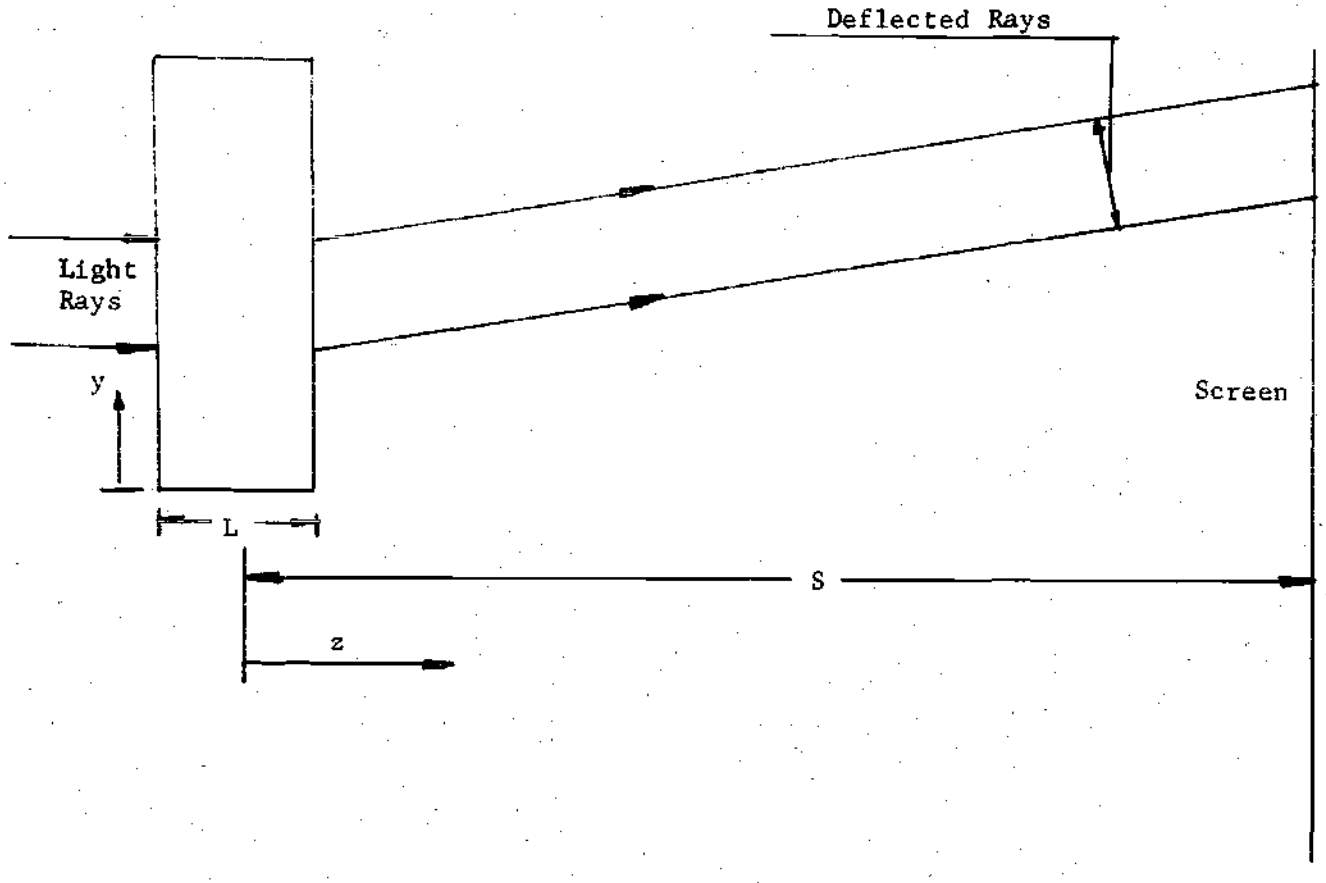

Figure 20. Schematic Diagram of a Shadowgraph System

Table 13. Relative Contrast, $\Delta I/I_0$, for Shadowgraphs with Measurements in Air

L/δ	y/δ	$\phi = \frac{T_w - T_a}{T_w}$		
		0.05	0.10	0.20
10.0	0.005	-2.39	-1.01	- 3.12
	0.01	-2.40	-1.019	- 3.25
	0.05	-2.54	-1.09	- 4.62
	0.10	-2.72	-1.18	- 8.67
	0.75	-5.90	-3.01	-12.19
	1.00	-6.4	-3.39	-20.47
5.0	0.005	-0.214	-0.143	- 0.233
	0.010	-0.214	-0.144	- 0.236
	0.05	-0.218	-0.149	- 0.258
	0.10	-0.223	-0.156	- 0.288
	0.75	-0.271	-0.231	- 0.809
	1.00	-0.276	-0.239	- 0.955
2.0	0.005	-0.029	-0.02	- 0.031
	0.010	-0.029	-0.02	- 0.031
	0.05	-0.029	-0.021	- 0.034
	0.10	-0.03	-0.022	- 0.037
	0.75	-0.035	-0.031	- 0.071
	1.00	-0.035	-0.031	- 0.084

Table 14. Relative Contrast, $\Delta I/I_0$, for Shadowgraphs with Measurements in Water

L/δ	y/δ	$\phi = \frac{T_w - T_a}{T_w}$		
		0.05	0.10	0.20
10.0	0.005	-4.6	-12.51	-26.36
	0.010	-4.6	-12.51	-26.36
	0.050	-4.57	-12.47	-26.33
	0.10	-4.54	-12.42	-26.21
	0.75	-4.27	-11.60	-22.37
	1.00	-4.25	-11.50	-21.84
5.0	0.005	-1.15	- 3.13	- 6.59
	0.010	-1.15	- 3.12	- 6.59
	0.050	-1.14	- 3.11	- 6.58
	0.10	-1.13	- 3.105	- 6.55
	0.75	-1.068	- 2.9	- 5.59
	1.00	-1.062	- 2.87	- 5.46
2.0	0.005	-0.18	- 0.5	- 1.05
	0.010	-0.18	- 0.5	- 1.05
	0.050	-0.18	- 0.49	- 1.05
	0.100	-0.18	- 0.49	- 1.049
	0.750	-0.171	- 0.464	- 0.895
	1.00	-0.17	- 0.46	- 0.873

Mach-Zehnder Interferometer

The third optical device for the measurement of temperature is the interferometer which is often used for quantitative studies. Interferometry, unlike Schlieren and the shadowgraph systems, does not depend upon the deflection of the light beam to determine the density distribution. In fact, the refraction effects are usually of second order and undesirable in the interferometers as they introduce deviations or errors in the evaluating equations. These errors have been evaluated in Chapter V.

In this section errors due to reading the fringe shift and calculations obtained from interferograms including the inaccuracy of fringe positions and improper extrapolation have been evaluated.

The Mach-Zehnder interferograms represent the temperature distribution field in the test section. However, to evaluate the heat transfer coefficient at the surface of the heated surface, the temperature gradient at the wall must be determined. Theoretically, it is necessary to approximate the temperature distribution by passing a polynomial through all available points near the surface wall and then determining a temperature gradient to this polynomial at the wall. For steady state studies, the temperature variation with distance measured perpendicular to the wall is often almost linear. Therefore, a straight line passing through these points near the wall is regarded as the temperature gradient at the wall. This leads to an error in the heat transfer evaluations.

In the absence of adequate experimental results, Goldstein's (10) calculations for run 05 and run R9, respectively, for air and water, were used for comparison. The evaluated values of θ as a function of the distance perpendicular to the wall were approximated by a third order poly-

nomial. The gradient to this polynomial at the wall was taken as a reasonably good approximation to the true value of the temperature gradient at the wall. This value of the temperature gradient was compared to the value of the temperature gradient evaluated by Goldstein. The difference expressed as a percentage of the true heat transfer coefficient at that location was evaluated as the error due to improper extrapolation. For run 05, this error was calculated to be 3.7 percent and for run R9, this error was 3.0 percent.

Differential Interferometer

The differential interferometer permits the measurements of the fringe shifts which are directly related to heat transfer measurements. Therefore, errors due to improper extrapolation do not exist for this type of instrument. However, due to the double image inherent in differential interferograms, the fringe shift obtained is the fringe shift that refers to heat transfer conditions at a distance, ΔX_s, away from the surface rather than those exactly at the wall.

In order to compare the evaluation errors observed in the Mach-Zehnder and differential interferometers, temperature profiles inside the boundary layer identical to those selected by Goldstein were assumed. The evaluation error was expressed as a percentage of the true heat transfer coefficient for the identical geometrical configuration as used in reference (10). This error was found to be 0.76 percent for air studies and 2.03 percent for water studies.

The analysis of various optical systems leads to the following conclusions:

1. Shadowgraph, Schlieren, and interferometric measurements are essentially integral ones in that they integrate the quantity measured over the length of the light beam. Hence, they are best suited for measurements in one or two dimensional fields where there is no variation in the refractive index in the direction of travel of the light beam with the exception of variations that exist at the entrance and exit regions of the test section.

2. Considering the Schlieren and shadowgraph systems, the relative contrast is higher for longer test sections. The same trend is observed when these systems are applied to both air and water. The sensitivity is higher for water studies than for air studies.

3. The sensitivity for the Schlieren systems as given by equation 31 is either positive or negative depending upon the position of the knife edge. Changing the position of the knife edge reverses the dark and light images on the screen. The brighter areas of the image represent regions in the test section where the density increases in the direction away from the knife edge. Dark areas represent regions where the density increases in the direction of the opaque side of the knife edge.

4. Because the minimum value of the contrast that can be easily evaluated is of the order of 0.05, the shadowgraph systems cannot be effectively employed for quantitative heat transfer measurements.

5. In the case of the Mach-Zehnder interferometer the evaluation error can be reduced by selecting a more accurate approximation equation for the temperature profile. This leads to a better extrapolation to obtain θ_w and k_f/h_x.

6. Comparing the evaluation errors in heat transfer measurements

for the Mach-Zehnder and differential interferometers, it is observed that the error is less by 79 percent for air studies and by 33 percent for water studies for the differential interferometer than the Mach-Zehnder interferometer. This suggests using the higher potential of the differential interferometer to predict accurate heat transfer coefficients for gases as well as liquids.

APPENDIX C

INTERFEROGRAM ANALYSIS AND SAMPLE CALCULATION

The fringe shift and thus the optical path difference between rays passing through the test section may be obtained directly from the parallel fringe interferogram. Figure 21 shows a sketch of a typical parallel fringe pattern produced by free convection from a flat plate. The fringe shift at the surface is a direct measurement of the local free convective heat transfer coefficient.

All of the steady state interferograms were analyzed using a metallurgical microscope. The microscope had a movable bed with a vernier least count of 0.004 inch. An eyepiece with a vertical cross hair and a magnification factor of 10X was used. The film was attached to the moving bed and was aligned so that the movement of the bed was parallel to the plate surface.

Usually the destructive fringes were used for the analysis. A desired fringe was located and its shift was traced under the microscope until the tail of the fringe merged with the plate surface. The number of the fringe shift was recorded. The distance of the fringe from the pointer was recorded. To determine the scale of the negative, the width of the scale-factor strip was also recorded.

For the infinite fringe pattern, the fringe represents the lines of the constant temperature gradient. The distance from the pointer and the scale factor were also determined.

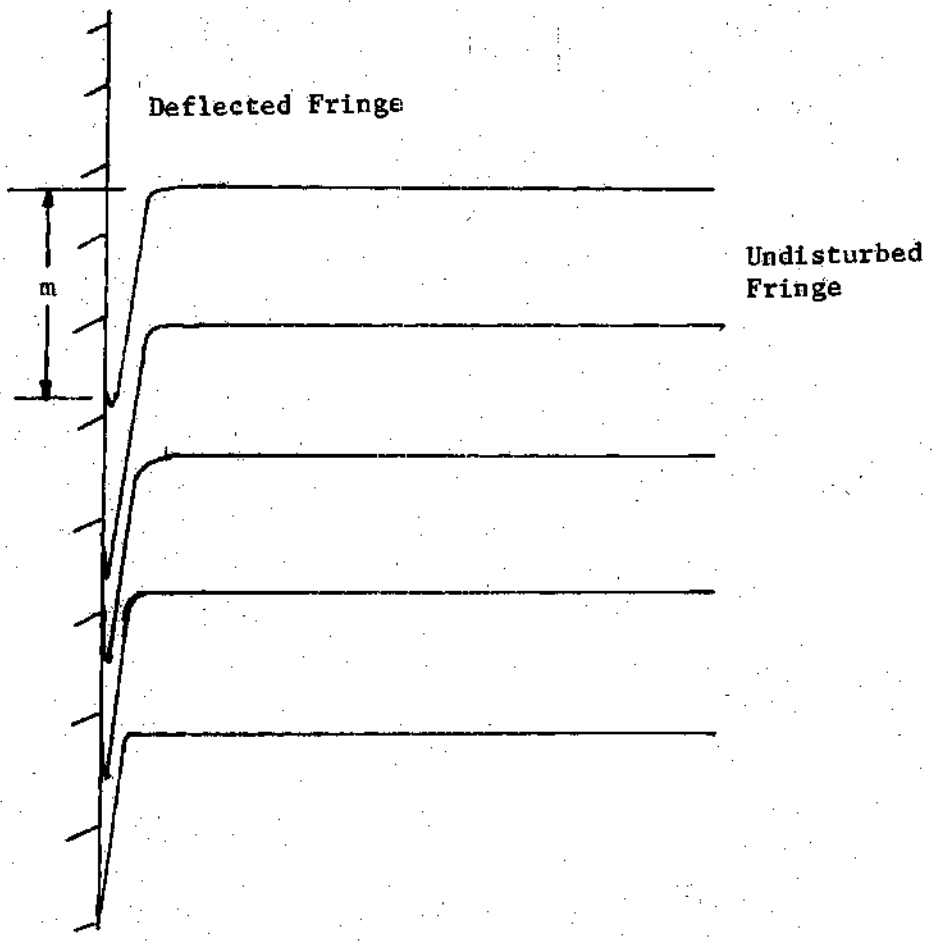

Figure 21. Schematic Diagram of a Parallel Fringe Pattern

Sample Calculation

Table 6 and Figure 22 show the temperature distribution on the plate for run 3a. The vertical bars in Figure 22 at certain locations show the crosswise temperature distribution at that elevation. As described in Chapter III, the average plate temperature was calculated to be 81.01°F. The average water temperature was 78.01°F.

The following interferometric parameters were constant for all the runs.

$\lambda = 5461$ Å

$\Delta n = 0.009165$

$L = 0.4167$ ft

$g = 3.280$ ft

$\theta_i = 0.01745$ radians

$dn/dy = 0.004095 \times m$ 1/ft

The temperature gradient of the index of refraction was calculated from equation 6:

$$dn/dT = - (118.73 + 41.4184T - 0.02376T^2 - 0.0043757T^3) \times 10^{-7}$$

$$= - 1140.49 \times 10^{-7} \text{ 1/°C}$$

$k_f = 0.3536$ Btu/hr-ft-°F

Substituting the above values into equation 6, the following relationship for h_x was obtained

$h_x = 7.64 \times m$, Btu/hr-ft^2-°F

The magnification factor for the film was 1.116 from which the exact location of the fringe was determined to be 0.8036 ft.

Table 15. Plate Temperature Data for Run 3a

T.C. #	M.V	°C	°F
1	1.062	26.8	80.24
2	1.096	27.6	81.68
3	1.075	27.1	80.78
4	1.095	27.6	81.68
5	1.090	27.5	81.50
6	1.076	27.1	80.78
7	1.095	27.6	81.68
8	1.087	27.4	81.32
9	1.079	27.2	80.96
10	1.090	27.5	81.50
11*	1.023	25.8	78.44
12*	1.020	25.8	78.44
13*	0.995	25.1	77.18

*Represent the ambient water temperature.

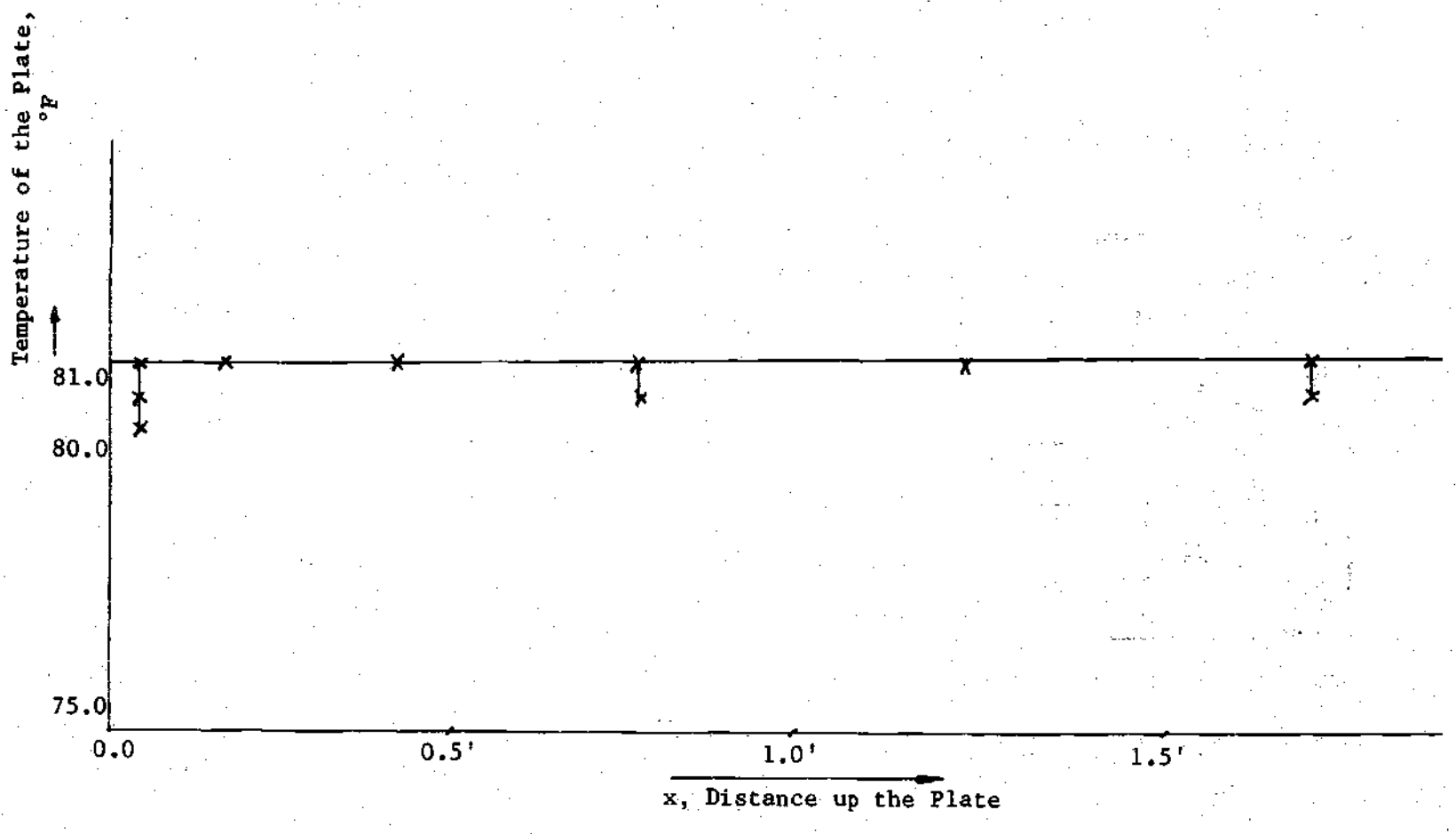

Figure 22. Temperature Distribution on the Plate for Run 3a

From the parallel fringe photograph the fringe shift was determined to be 4.12. This gave the local value of the heat transfer coefficient as 31.4768 Btu/hr-ft^2-°F and the local value of the Nusselt number as 71.535. The local value of the Rayleigh number evaluated at the film temperature was 5.07×10^8.

APPENDIX D

HEAT TRANSFER RESULTS

Table 16. Data for Figures 8 and 9

x ft	Rayleigh Number	Experimental $Nu_x/[Ra_x]^{0.25}$	Theoretical $Nu_x/[Ra_x]^{0.25}$ Ref. (25)	Percent Variation
0.1590	3.61×10^6	0.448	0.488	- 8.10
0.2502	1.4×10^7	0.461	0.489	- 5.72
0.2779	2.5×10^7	0.456	0.486	- 6.1
0.3680	1.04×10^8	0.430	0.483	-11.0
0.677	4.09×10^8	0.494	0.488	+ 1.02
0.6773	4.097×10^8	0.493	0.488	+ 0.86
0.6820	4.94×10^8	0.443	0.483	- 8.20
0.7210	4.96×10^8	0.489	0.488	+ 0.05
0.7217	4.97×10^8	0.470	0.466	+ 0.85
0.7300	6.17×10^8	0.443	0.460	- 3.6
0.7800	7.31×10^8	0.486	0.484	+ 0.41
0.8036	5.07×10^8	0.476	0.484	- 1.60
0.8070	8.02×10^8	0.497	0.492	+ 0.962
0.8720	8.79×10^8	0.500	0.488	+ 1.12
1.0915	1.73×10^9	0.510	0.489	+ 4.2
1.0915	2.85×10^9	0.461	0.487	- 5.3

Table 17. Heat Transfer Results at Higher Temperature Conditions Where Refraction is Significant

x ft	$T_w - T_a$ (°F)	T_w (°F)	Experimental $Nu_x/[Ra_x]^{0.25}$	Theoretical $Nu_x/[Ra_x]^{0.25}$ Ref. (25)	Percent Variation
0.159	2.45	84.25	0.448	0.488	- 8.10
0.1694	3.78	88.88	0.214	0.488	-56.1
0.1827	4.73	96.13	0.158	0.488	-67.6
0.278	3.24	84.02	0.494	0.488	+ 1.02
0.3076	4.25	92.47	0.226	0.486	-53.5
0.3061	6.91	97.87	0.109	0.486	-77.5

Table 18. Heat Transfer Results in Transitional and Turbulent Regime

x ft	$T_w - T_a$ (°F)	T_w (°F)	Experimental Nu_x	Local Rayleigh Number
1.065	3.04	79.88	134.8	1.16×10^9
1.071	8.23	98.13	36.91	4.85×10^9
1.5316	3.015	81.095	153.96	4.91×10^9
1.5474	2.14	91.205	141.33	3.75×10^9
1.5844	3.015	81.095	148.24	5.40×10^9
1.6833	4.710	99.83	49.025	1.14×10^{10}
1.520	7.93	105.93	71.90	1.63×10^{10}

Table 19. Frequency Measurement Data

Time Min (Ti)	Strength	No. of Waves	Tj = (Ti+1-Ti)	f = 1/Tj
0.00	4	1	0.00	
5.40	3	1	5.40	0.186
18:50 - 8:55	2	2-3	3.10	0.32
10:27	3	1	1.7	0.58
15:32 - 15:40	3-2	3	2.7	0.37
17.5 - 17.75	3---2	4	2.1	0.47
19.10	3-3	2	1.6	0.62
20.5	3	2	1.4	0.71
21.16 - 21.5	4---2	4	0.8	1.25
23.16 - 23.3	4---3	3	2.0	0.31
25.4	4-4	2	1.75	0.57
26.75	4-4	3	1.35	0.74

BIBLIOGRAPHY

1. Lorenz L., Wiedemanns Annalen 147, 429 (1872).

2. Schmidt E. and Beckman W., "Das Temperature and Geschwindigkeits-feld Platte bei Naturlicher Konvection," Techniche Mechanik und Thermodynamik 1 (Oct. 1930), 341-349.

3. Polhausen E., Zeitschr. f. agnew Math. u. Mech. 1, 115 (1921).

4. Saunders O. A., "Natural Convection in Liquids," Proc. Royal Society (London), Series A, 157 (1936).

5. Eckert E.R.G. and Jackson T.W., "Analysis of turbulent free convection boundary layer on a flat plate," NACA Report, 1015.

6. Ostrach S., "An Analysis of Laminar Free-Convection Flow and Heat Transfer about a Flat Plate Parallel to the Direction of the Generating Force," NACA Report, 1111.

7. Ezer Griffiths and Davis A.H., "The Transmission of Heat by Radiation and Convection," Special Report No. 9, Food Investigation Board; British Dept. Sci. and Ind. Res. (1922).

8. Dotson J.P., "Heat Transfer from a Vertical Plate by Free Convection," M.S. Thesis, Purdue University (May 1954).

9. Fujii Tetsu, "Experimental Studies of Free Convection Heat Transfer," Bulletin of J.S.M.E. 2:8 (1959).

10. Goldstein R.J., "Interferometric Study of the Steady State and Transient Free Convection Boundary Layers in Water about a Uniformly Heated Vertical Flat Plate," Ph.D. Thesis, University of Minnesota (March 1959).

11. Eckert E.R.G., "Interferometric Studies of Beginning Turbulence in Free and Forced Convection Boundary Layers on a Heated Plate," Preprint of Papers, Heat Transfer and Fluid Mechanics Institute (1949), pp. 181-190.

12. Szewczyk Albin A., "Stability and Transition of the Free Convection Layer Along a Vertical Flat Plate," International Journal of Heat and Mass Transfer 5 (1962), pp. 903-914.

13. Lock G.S.H. and Trotter F.J.Deb., "Observations on the Structure of a Turbulent Free Convection Boundary Layer," International Journal of Heat and Mass Transfer 11 (1968)

BIBLIOGRAPHY (Continued)

14. Black Clifford P., "The Thermal Structure of Free Convection Turbulence from an Inclined Flat Plate and Its Influence on Heat Transfer," M.S. Thesis, Georgia Institute of Technology (August 1974).

15. Azami B., "Determination of the Temperature Distribution in a Water Film Adhering to a Vertical Heated Surface and the Local Heat Transfer Coefficient by Interferometry," M.S. Thesis, University of Maryland (1956).

16. Bryngdahl O., "The Accurate Estimation of the Thermal Conductivity Properties in Liquids by Means of a Shear Interferometric Method," Arkiv for Fysik 21, Paper 22 (1962).

17. Black Wm. Z. and Carr W.W., "Application of a Differential Interferometer to the Measurement of Heat Transfer Coefficients," The Review of Scientific Instruments 42 (1971), pp. 337-340.

18. Black Wm. Z. and Carr W.W., "A Differential Interferometer and Its Application to Heat and Mass Transfer Measurements," ASME Paper No. 72-Ht-12, presented at the ASME-AIChE Transfer Conference, Denver, Colorado, August 1972.

19. Black Wm. Z. and Norris, J.K., "Interferometric Measurement of Fully Turbulent Free Convective Transfer Coefficients," The Review of Scientific Instruments, 45:2, 216-218 (1974).

20. Brodowicz K., "An Analysis of Laminar Free Convection Around Isothermal Vertical Plate," International Journal of Heat and Mass Transfer, 11:2, 201-209 (1968).

21. Osborn Fredrick A., "Change of Index of Refraction of Water with a Change of Temperature," Phys. Rev., 1, 208 (1913).

22. Tilton L.W. and Taylor J.K., "Refractive Index and Dispersion of Distilled Water for Visible Radiation at Temperatures 0°C to 60°C," Journal of the Research of the N.B.S., 20, 419 (April 1938).

23. Tilton L.W. and Taylor J.K., "Accurate Representation of the Refractivity and Density of Distilled Water as a Function of Temperature," Research Paper RP971, Journal of Research of the N.B.S., 18 (February 1937).

24. Carr W.W., "The Measurement of Instantaneous, Local Heat Transfer from a Horizontally Vibrating Isothermal Cylinder Using a Differential Interferometer," Ph.D. Thesis, Georgia Institute of Technology (March 1973).

BIBLIOGRAPHY (Continued)

25. Sparrow E., "Laminar Free Convection on a Vertical Plate with Prescribed Non-uniform Wall Heat Flux or Prescribed Non-uniform Wall Temperature," NACA TN 3508 (July 1955).

26. Vliet C.G., "Natural Convection Local Heat Transfer on Constant Heat Flux Inclined Surfaces," ASME Paper No. 69-Ht-C (1969).

27. Vliet C.G. and Liu C.K., "An Experimental Study of Turbulent Natural Convection Boundary Layers," ASME Journal of Heat Transfer, 91, 577 (1969).

28. Sernas V, Fletcher L.S., and Aung W., "Heat Transfer Measurements with a Wollaston Prism Schlieren Interferometer," ASME Paper No. 72-Ht-9, Presented at the ASME-AIChE Heat Transfer Conference, Denver, Colorado, August 1972.

29. Goldstein R.J., "Optical Measurement of Temperature," in Measurement Techniques in Heat Transfer; Editors Eckert E.R.G. and Goldstein R.J.; Publishers: Technivision Services Slough, England, November 1968.

30. Wachtell G., "Refraction Error in Interferometry of Boundary Layers in Supersonic Flow Along a Flat Plate," Ph.D. Thesis, Princeton University (1951).

31. Eckert E. and Soehngen E., "Distribution of Heat Transfer Coefficients Around Circular Cylinders in Cross Flow at Reynolds Numbers from 20 to 500," Trans. ASME, 74, 343 (1952).

32. Howes W. and Buchele D., "Practical Considerations in Specific Applications of Gas-Flow Interferometry," NACA TN 3507 (July 1952).

33. Eckert E.R.G. and Drake Robert M., "Analysis of Heat and Mass Transfer," McGraw-Hill Company; First Edition, 1972.

34. Kreith Frank, "Principles of Heat Transfer," Intext Educational Publishers, Third Edition, 1973.

35. Sparrow E. and Gregg J., "Variable Fluid Property in Free Convection," Transactions ASME, 50, 879 (1958).

36. Sparrow E., "Free Convection with Variable Properties and Variable Wall Temperature," Ph.D. Thesis, Howard University (May 1956).

37. Cheneveau Charles, "Refractivity of Selected Solids and Liquids," International Critical Tables, Volume VII.

BIBLIOGRAPHY (Concluded)

38. Eckert E.R.G. and Soehngen E., "Interferometric Studies on Stability and Transition to Turbulence of a Free Convection Boundary Layer," General Discussion on Heat Transfer, September 1951, pp. 321-323.